Hunting for the Primordial Quenched Population in $2 < z < 2.5$ COSMOS Protoclusters

by

Adit Harin Edward

A thesis
presented to the University of Waterloo
in fulfillment of the
thesis requirement for the degree of
Master of Science
in
Physics

Waterloo, Ontario, Canada, 2023

Author's Declaration

This thesis consists of material all of which I authored or co-authored: see Statement of Contributions included in the thesis. This is a true copy of the thesis, including any required final revisions, as accepted by my examiners.

I understand that my thesis may be made electronically available to the public.

Statement of Contributions

This thesis is based on the following paper:

Edward A. H., Balogh M. L., Bahé Y. M., Cooper M. C., Hatch N. A., Marchioni J., Muzzin A., Noble A., Rudnick G. H., Vulcani B., Wilson G., De Lucia G., Demarco R., Forrest B., Hirschmann M., Castignani G., Cerulo P., Finn R. A., Hewitt G., Jablonka P., Kodama T., Maurogordato S., Nantais J., Xie L., 2024. The stellar mass function of quiescent galaxies in $2 < z < 2.5$ protoclusters. *Monthly Notices of the Royal Astronomical Society*, Vol. 527, Issue 3, pp. 8598-8617. doi: 10.1093/mnras/stad3751

I was the first author of this paper, and performed most of the analysis and writing of this paper. This research was done under the supervision of Dr. Michael Balogh who guided this project, as well as heavily edited the writing of the paper. This research also benefitted from the contributions and consultations from the ISSI collaborators listed as coauthors on this paper, as well as from Guillaume Hewitt and Justin Marchioni. These contributions were largely in the form of writing edits, but also include group and one-on-one discussions that helped further this project.

This research makes use of the COSMOS2020 catalogue (https://cosmos.astro.caltech.edu/).

Fig 1.1 was taken from Girelli et al. (2020), Fig 1.2 from van der Burg et al. (2020), and Fig 1.3 from Overzier (2016).

All other work in this thesis is my own.

Abstract

We present an analysis of the galaxy stellar mass function (SMF) of 14 known protoclusters between $2.0 < z < 2.5$ in the COSMOS field, down to a mass limit of $10^{9.5}$ $M_\odot$. We use existing photometric redshifts with a statistical background subtraction, and consider star-forming and quiescent galaxies identified from $(NUV - r)$ and $(r - J)$ colours separately. Our fiducial sample includes galaxies within 1 Mpc of the cluster centres. The shape of the protocluster SMF of star-forming galaxies is indistinguishable from that of the general field at this redshift. Quiescent galaxies, however, show a flatter SMF than in the field, with an upturn at low mass, though this is only significant at $\sim 2\sigma$. There is no strong evidence for a dominant population of quiescent galaxies at any mass, with a fraction $< 15\%$ at 1σ confidence for galaxies with $\log M_*/M_\odot < 10.5$. We compare our results with a sample of galaxy groups at $1 < z < 1.5$, and demonstrate that a significant amount of environmental quenching must take place between these epochs, increasing the relative abundance of high-mass ($M_* > 10^{10.5} M_\odot$) quiescent galaxies by a factor $\gtrsim 2$. However, we find that at lower masses ($M_* < 10^{10.5} M_\odot$), no additional environmental quenching is required.

Acknowledgements

First and foremost, I would like to thank my supervisor, Dr. Michael Balogh. The guidance, support and advice given by him was incredibly helpful and important to the success of this project and my growth as a researcher. The opportunities I have been afforded during the course of my MSc have given me memories that will last me a lifetime, and I cannot thank you enough for that. Coming to do my MSc in Waterloo has been a great experience, and in no small part is that because I have had a supervisor whom has been amazing to work with.

Thank you as well to all my collaborators that have helped with writing my paper. Despite my being the most junior researcher at our telecons and in person meetings, I was always made to feel welcome. The help and advice given for my research and paper have been incredibly helpful, and I feel extremely proud of the work we have done together.

I would also like to thank my family and friends for their continued support, with a special thanks to my parents and my sister. I know my chaotic schedule has left me largely unavailable the last number of years, but I hope to make that up to you all soon. A few of you have asked how I manage all that I do, and the answer is because of the support you all give me- I wouldn't be able to otherwise.

Dedication

To Grandma, Grandpa, Ammamma and Sri Lankan Grandma & Grandpa- thank you for all that you've done for me, and for all you have taught me. I hope I've made you proud, and continue to do so. I miss you all more than I could ever put in words.

Table of Contents

List of Figures

List of Tables

Chapter 1

Introduction

For the past $\sim$ 20 years, ΛCDM has been widely considered the best model to describe our universe and how it evolved through time (Peebles, 1984; Carroll, 2001; Peebles & Ratra, 2003). It is a well-defined model with clear predictions for the early state and large-scale structure of the universe. While there exist many tensions and challenges (see Bull et al., 2016; Turner, 2022; Peebles, 2022; Perivolaropoulos & Skara, 2022, for reviews), it remains very successful at describing the cosmic microwave background (CMB) (Page et al., 2003), the chemical abundances of hydrogen, deuterium and helium (Fields, 2011), the cosmic acceleration of the universe (Perlmutter et al., 1999; Riess et al., 1998), and the large-scale structure we observe today (Zehavi et al., 2005; Bernardeau et al., 2002).

The ΛCDM model rests on a few basic tenets. The first is that the universe is composed of three main components: radiation, matter and dark energy (Zwicky, 1933, 1937; Rubin & Ford, 1970; Rubin et al., 1980; Bertone et al., 2005). The radiation component is from photons and neutrinos, while the matter component is split between ordinary (baryons and leptons) matter and cold dark matter. The dark energy component is often denoted by Λ as the cosmological constant (Carroll et al., 1992; Carroll, 2001), and is considered to be the cause for the accelerated expansion observed in the last $\sim$5 billion years. The Planck 2018 results showed that $\sim$ 31.5% of the universe is made up of matter, and about $\sim$ 68.5% of the universe is made up of dark energy (Planck Collaboration et al., 2020). In general, the Planck Collaboration et al. (2020) results are in strong agreement with a ΛCDM model. This is shown in the match between the predicted and observed temperature power spectrum.

The ΛCDM model assumes that on cosmological scales, General Relativity (GR) (Einstein, 1917) is the best descriptor of gravity. It should be noted that this has yet to be

reconciled with quantum mechanics, but is otherwise the best model we have to explain the observed behaviour of gravity. Additionally, the third tenet of the ΛCDM model is the cosmological principle. This principle is the assumption that on scales sufficiently large ($\gtrsim$ 100 Mpc), the universe is both homogeneous and isotropic. This was first presented in Newton (1687), and despite some claims of anisotropy (e.g, Migkas et al., 2020; Secrest et al., 2021) and inhomogeneity (e.g, Gott et al., 2005; Horvath et al., 2013), this remains a standard assumption.

The main consequence of the cosmological principle with GR is the Freidmann-Lemaître-Roberson-Walker (FLRW) metric. This metric, in combination with Einstein's field equations, gives the Friedmann equations, which describe the growth and acceleration of the universe (Friedmann, 1922).

While not a part of the ΛCDM model, it is also often assumed that a period of rapid acceleration known as inflation took place. This inflation is assumed to solve the horizon and flatness problems otherwise found in the ΛCDM model (Starobinsky, 1980; Guth, 1981; Albrecht & Steinhardt, 1982; Linde, 1982).

One of the main predictions of the ΛCDM model is hierarchical structure formation (White & Frenk, 1991). This prediction describes the growth of large-scale structure in the universe as hierarchical, first forming galaxies, then clusters, and then the superclusters still forming today (e.g. Cucciati et al., 2018; Tully et al., 2014; Kravtsov & Borgani, 2012). That is to say, small-scale structure such as galaxies can form at all redshifts, but the scale of the largest structures in the Universe increase over time. In the early universe, small quantum fluctuations were amplified by the aforementioned cosmic inflation. This grew the fluctuations into regions of over- and under-densities. As this was prior to matter-radiation equality, radiation pressure dominated. Because dark matter doesn't feel radiation pressure, it fell in first, creating dark matter halos (Turner, 2022). As the universe expanded and cooled, neutral hydrogen was eventually able to form by the capture of electrons by protons during a period called 'recombination'. The photon decoupling this produced then became what we now observe to be the CMB. The decoupling of matter from photons allowed baryonic matter to also follow dark matter and flow into the potential wells.

After recombination, structure was formed via both gradual accretion and mergers in a bottom-up manner (White & Frenk, 1991). That is to say, smaller halos formed first, then forming larger and larger halos. The growth and distribution of these dark matter halos has been modelled by the halo mass function (HMF), famously first introduced by Press & Schechter (1974). In the years since, both simulations and observations have been used to study the HMF and its evolution through redshift. The HMF is perhaps the best way to show hierarchical structure formation, as we observe the build up of massive systems over

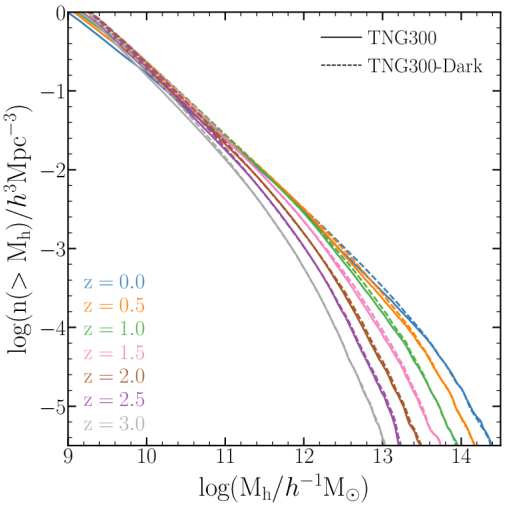

Figure 1.1: The cumulative halo mass functions for TNG300 (solid lines) and TNG300-dark (dashed lines), taken from (Contreras & Zehavi, 2023). The build up of large halos in these simulations between $z = 3$ to $z = 0$ is shown. For example, at $z = 3$, the number density of halos with a halo mass $\mathrm{M_h} > 10^{13}\mathrm{M_\odot h^{-1}}$ is $\sim 10^{-5.2} h^{-3}\mathrm{Mpc}^{-3}$. By z=0, this rises to $\sim 10^{-3.2} h^{-3}\mathrm{Mpc}^{-3}$.

time. We show the HMF from simulations in Fig 1.1. These simulations come from the IllustrisTNG (Pillepich et al., 2018; Nelson et al., 2019) suite. TNG300 is the ∼300 Mpc^3 volume simulation, the largest of the Illustris runs. It is an N-body simulation, with the intial conditions based on the latest cosmology models. It uses Newtonian gravity with a FLRW model as well. TNG300-dark is the dark matter only counterpart to TNG300.

The distribution of large structure in the universe is called the 'cosmic web' (Bond et al., 1996). This cosmic web is made up of large voids, walls, filaments and nodes. Voids are massive, (roughly) spherical structures, reaching diameters of $\sim$ 100 Mpc (Carroll & Ostlie, 1996) and make up most of the volume in the observable universe (Pan et al., 2012). They are also extraordinarily underdense regions, containing little to no galaxies within them (Peebles, 2001). Surrounding these massive voids are walls (Bharadwaj et al., 2004), large, overdense regions that were first observed in Geller & Huchra (1989). These walls are thin and extended (Peebles, 2001), containing dense filaments, which stretch out for tens of Mpc (Bond et al., 1996; Pan et al., 2012). Most galaxies lie in these filaments. At the intersections of these filaments are nodes, generally hosting massive halos. These massive halos are typically galaxy clusters or groups.

In hierarchical structure formation, galaxy clusters form from the assembly of the less

massive groups and individual galaxies, both through simple accretion and mergers (White & Frenk, 1991). They host an abundance of elliptical galaxies, centered on a massive brightest cluster galaxy (BCG). They are are massive structures, typically having masses between $10^{14} - 10^{15} M_{\odot}$. They are made up of hundreds, sometimes even thousands, of galaxies, all bound together in a gravitational well. The gas in these clusters is known as the intracluster medium (ICM). This gas is much hotter than the intergalactic medium (IGM) typically found between galaxies. The ICM is thought to be heated via gravitational heating (e.g, Kaiser, 1986; Dong et al., 2023), feedback from active galactic nuclei (AGN) (Yang & Reynolds, 2016), and the merging of subhalos within the cluster (Zuhone & Markevitch, 2009). The high temperature of this gas causes it to emit brightly via the bremsstrahlung effect in the x-ray.

While galaxies form via the cooling of gas in dark matter halos (Cole & Lacey, 1996; Kauffmann et al., 1993) as predicted by hierarchical structure formation, the evolution of the stellar mass function (SMF) reveals complications with this picture. Observations of the SMF have demonstrated that massive galaxies formed earlier, followed by lower mass galaxies over time (e.g. Dickinson et al., 2003; Rudnick et al., 2003, 2006; Ilbert et al., 2013; Muzzin et al., 2013; Davidzon et al., 2017; Leja et al., 2020; McLeod et al., 2021; Santini et al., 2022; Weaver et al., 2022a; Taylor et al., 2023). These same studies have also shown that most of the stellar mass in the Universe forms by $z \sim 2$. When looking at just star-forming galaxies, the shape of the SMF evolves weakly after this point. This means that growth via star formation must cease for a significant number of galaxies. This process, known as quenching, leads to a gradual accumulation of non-star forming, passively-evolving galaxies (also known as quiescent galaxies).

Peng et al. (2010) showed that the evolution of SMFs over $0 < z < 2$ can be matched by an empirical model in which galaxies quench with a probability that is proportional to their star formation rate (SFR). Other authors have shown that this can be achieved with a quenching probability that is more fundamentally related to halo mass (Dekel & Birnboim, 2006). This empirical model is often referred to as mass quenching, and is likely driven in part by energy injection due to AGN (Silk & Rees, 1998; Hopkins et al., 2006) and supernova feedback (Dekel & Silk, 1986; Ceverino & Klypin, 2009).

Galaxies are also affected by their environment (Dressler, 1980), and processes like ram pressure stripping (Gunn & Gott, 1972; Poggianti et al., 2017), starvation (Larson et al., 1980; Balogh et al., 2000) and galaxy mergers (Springel et al., 2005) can lead to environmental quenching and an excess fraction of passive galaxies in high-density regions (e.g. Blanton et al., 2005; Wetzel et al., 2012), such as galaxy clusters (Lewis et al., 2002; Gómez et al., 2003) and galaxy groups (McGee et al., 2011).

Effects like ram pressure stripping and starvation are caused by the influence the ICM has on the galaxies in the cluster. Ram pressure stripping describes the removal of gas due to the high pressure the ICM exerts on galaxies travelling at high velocities. This pressure is proportional to ρv^2, where ρ is the density of the ICM in question, and v is the velocity of said galaxies with respect to the ICM (Gunn & Gott, 1972). The cool gas within these galaxies gets quickly ($\lesssim 0.5-1$ Gyr; Boselli et al., 2022) removed, quenching these galaxies (Boselli et al., 2022). This pressure can only remove gas from galaxies if it exceeds the restorative force, and is hence why it is more effective at quenching smaller galaxies which have a lower restoring force. The stripping of gas from the galactic disks can leave behind a trail of this gas behind the infalling galaxy. These galaxies are known as 'jellyfish galaxies' (e.g., Smith et al., 2010; Ebeling et al., 2014), and are a prominent feature in galaxy clusters, particularly in the cores ($r < 0.5R_{200}$), travelling at very high velocities ($v \gtrsim 2000$km/s) (Roberts et al., 2021). This is in contrast to galaxy starvation (also known as strangulation), where the IGM gas gets accreted onto the central potential of the cluster (the BCG) instead of the individual satellite galaxies (Larson et al., 1980; Balogh et al., 2000). This starves the satellite galaxies, and the gas already present in the galaxy is slowly depleted. The SFR of the satellite then slowly diminishes before becoming quenched over a few Gyrs (Balogh et al., 2000).

Galaxy interactions also play an important role environmental quenching. Galaxy mergers are known to trigger large amounts of star formation, reaching a 'starburst' phase where the SFR reaches or even surpasses 100 $M_\odot$/yr. This depletes the gas reservoir, causing the descendent galaxy to be quiescent (Mihos & Hernquist, 1994). This depletion typically takes ~ 0.5 Gyr (Muzzin et al., 2012; Belli et al., 2019), though there is substantial uncertainty associated with this number. Galaxy harassment, on the other hand, involves the tidal disruptions due to the gravitational effects of two galaxies passing by each other. These disruptions can enhance star formation, again causing the gas reservoir to deplete. This has been shown to be more common for galaxies with elliptical orbits within clusters (Moore et al., 1996). Galaxy harassment is thought to be the dominant quenching mechanism within ~ 50 kpc of the cluster centers (Moore et al., 1996, 1998, 1999), as well as being more effective at quenching lower mass satellite galaxies (Moore et al., 1999). It takes several crossing times for this to take effect (Boselli & Gavazzi, 2006).

Baldry et al. (2006) and Peng et al. (2010) showed that the fraction of quenched galaxies at $z = 0$ depends separably on mass and environment. The simplest interpretation is that the effectiveness of environmental quenching is independent of galaxy mass. However, observations have shown that this separability does not hold at higher redshifts (e.g. Kawinwanichakij et al., 2017; Pintos-Castro et al., 2019). For example, an analysis of clusters at $0.8 < z < 1.5$ in the GCLASS (Gemini CLuster Astrophysics Spectroscopic Survey)

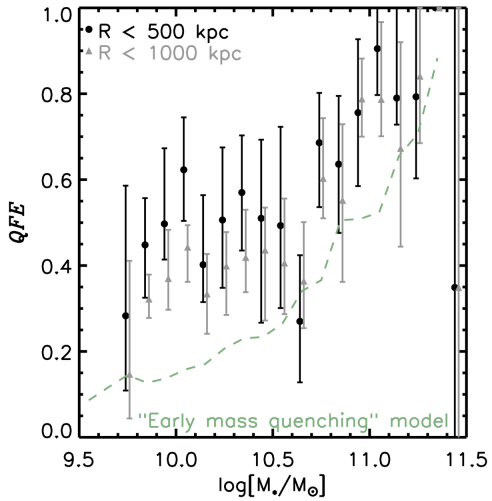

Figure 1.2: The quenched fraction excess (QFE) as a function of mass for clusters at $0.8 < z < 1.5$ from GOGREEN and GCLASS, taken from van der Burg et al. (2020). The QFE is a measure of how efficient an environment is at quenching galaxies relative to the field. A clear mass dependence is apparent, implying the results from Peng et al. (2010) does not hold at higher redshift. The green dashed line shows a model of galaxy evolution where field and cluster galaxies form at different redshifts.

and GOGREEN (Gemini Observations of Galaxies in Rich Early Environments) surveys (Balogh et al., 2021) shows that the excess quenched fraction in clusters relative to the field is strongly mass dependent (Balogh et al., 2016; van der Burg et al., 2020). We show this in Fig 1.2. In particular, for massive galaxies only, the excess of quenched galaxies relative to the field is as high as it is in the local Universe. The stellar populations in these galaxies are also very old (Webb et al., 2020), indicating that they likely ceased forming stars long before they were part of a rich cluster. This is consistent with earlier work by Thomas et al. (2005), who show that most star formation in early-type galaxies located in high-density environments is expected to have happened between $3 < z < 5$. This may partly be attributed to a "preprocessing" that occurs in groups and filaments long before galaxies are accreted into massive clusters (e.g. Reeves et al., 2021; Werner et al., 2022). Alternatively, or in addition, there may be a "primordial" population of massive quiescent galaxies that were formed during the very earliest stages of cluster assembly (see also Poggianti et al., 2006). For quiescent galaxies with lower stellar mass, $\lesssim 10^{10.5}$ $M_\odot$, there is strong evidence that their star formation ceased much later, upon first infall into a massive cluster (Muzzin et al., 2014; McNab et al., 2021), leading to a more gradual build up of quiescent galaxies in clusters (e.g. Gilbank & Balogh, 2008). Alternatively, Baxter et al. (2022, 2023) showed that an accretion-based quenching model could work at all masses if the quenching timescale is dependent on mass, such that massive galaxies quench more quickly and earlier than less massive galaxies.

By definition, primordial quenching would have occurred within protoclusters – the overdense, pre-virialized volumes at $z \gtrsim 2$ that will eventually collapse and form massive clusters. These volumes are very large ($\sim 10^3 - 10^4 \mathrm{cMpc}^3$; Chiang et al., 2013, 2017; Lovell et al., 2018) , and are only modestly overdense (Muldrew et al., 2015; Chiang et al., 2017) relative to modern-day clusters. Despite this, the populations of protoclusters are very important for our understanding of both present-day clusters, as well as structure formation (Overzier, 2016). These volumes are the largest overdensities in the early universe ($z \gtrsim 2$) by definition, and are often found in dense, gas-rich filaments in the cosmic web (Overzier, 2016).

Recent simulations tell us that at $z \sim 2$, protoclusters make up ∼20% of the total SFR density of the universe, and 50% at $z = 10$ (Chiang et al., 2017). From $z \sim 10$ to $z \sim 5$ they grow inside-out, developing their core and its associated halo as extremely active regions (Chiang et al., 2017). By the end of this phase, the halo reaches a peak star formation efficiency (SFE) (Wechsler & Tinker, 2018) when they approach a mass of $\sim 10^{12} M_\odot$ (Chiang et al., 2013). From $z \sim 5$ to $z \sim 1.5$, there is high SFR (total SFR $\gtrsim 1000 M_\odot \mathrm{yr}^{-1}$) for galaxies throughout the protocluster (e.g, Geach et al., 2005; Casey, 2016; Popescu et al., 2023), growing the surrounding halo (Chiang et al., 2017; Popescu

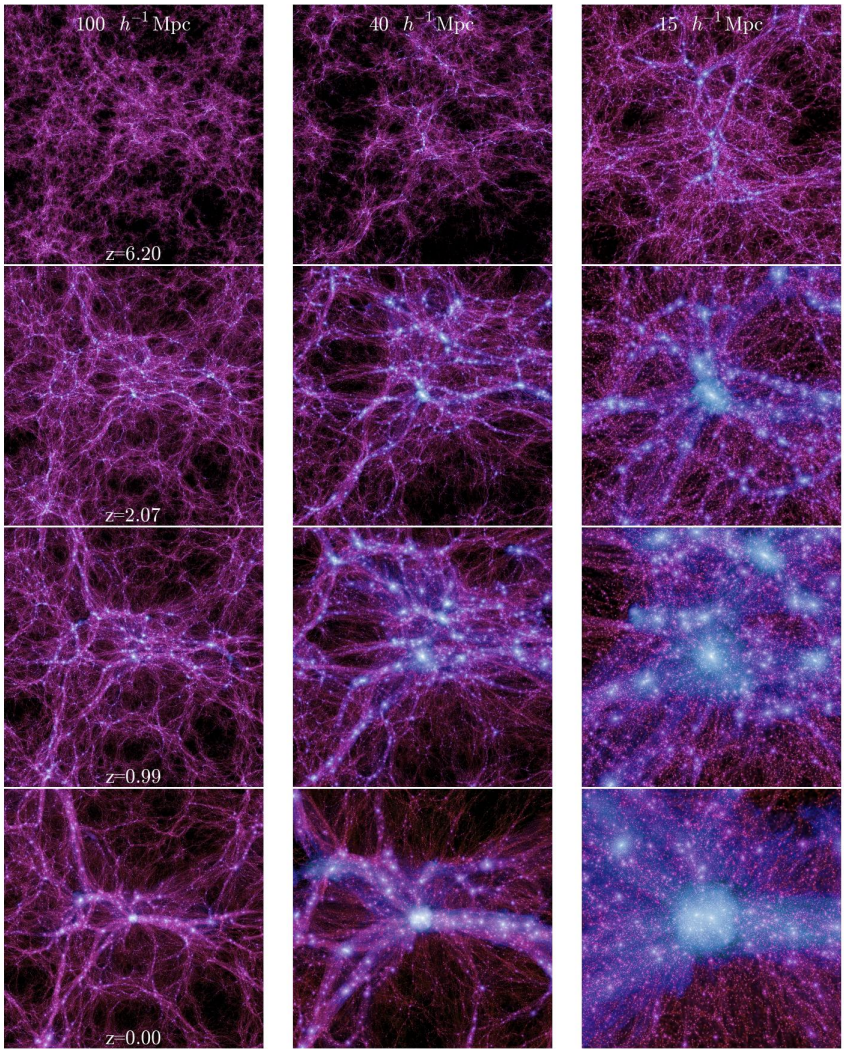

Figure 1.3: Growth of a galaxy cluster in the Millennium II dark matter simulation, taken from Overzier (2016), originally produced in Boylan-Kolchin et al. (2009). Panels show the growth of the cluster on different scales (left-to-right, 100, 40 and 15 h^{-1}Mpc) throughout redshift (top-to-bottom, $z = 6.20, 2.07, 0.99$ and 0). This shows the overdensity is present as early as $z \sim 6$ on the scale of a few dozen h^{-1}Mpc, in line with expectations from simulations (e.g, Chiang et al., 2017).

et al., 2023) which reaches the peak SFE (Chiang et al., 2017). During this time, $\sim 65\%$ of the stellar mass observed at $z = 0$ clusters is grown (Chiang et al., 2017). Observations show that at a fixed stellar mass, galaxies in protoclusters have higher SFR (Casey, 2016). After this time, protoclusters collapse into the modern day clusters, quenching throughout the volume. During this last stage, the protocluster undergoes dynamical relaxation and virialization, erasing some of the indicators of its formation history (Zabludoff et al., 1996; Kodama et al., 2001).

Direct observation of the galaxy population in these regions is required to decouple the primordial quiescent population from later accretion-driven quenching. This is challenging, as it requires a survey of galaxies over a wide area that is unbiased (e.g. with respect to SFR and dust content) down to a sufficiently low stellar mass in order to study the regime at which accretion-driven quenching is dominant. The most accurate way to identify protocluster members is by exploiting a highly complete, deep spectroscopic survey above $z > 2$, which does not yet exist. Though there have been spectroscopic observations of protoclusters above this redshift (e.g., Yuan et al., 2014; Lee et al., 2016; Wang et al., 2016; Diener et al., 2015; Darvish et al., 2020; McConachie et al., 2022; Ito et al., 2023), these are insufficient in completeness, spatial extent and depth. The alternative is to use photometric redshifts. The larger uncertainties associated with these redshifts, however, mean large samples are required so that the signal from these modest overdensities can be extracted in the presence of a dominant background.

For this reason we use the data from The Cosmic Evolution Survey (COSMOS, Scoville et al., 2007), the survey with the best photometric redshifts over a cosmologically significant area. More specifically, we take advantage of the deep (~ 26 AB) multi-band photometry from the COSMOS2020 catalogue (Weaver et al., 2022b, hereafter W22), covering ~ 2 deg^2. In this thesis, we analyze the SMFs of quiescent and star-forming galaxies within 14 previously identified protoclusters in this field, selected from the catalogue of Ata et al. (2022) to be at $2.0 < z < 2.5$. In constructing the SMFs we largely follow the methodology described in (Weaver et al., 2022a, hereafter W23).

This thesis is structured as follows. In Chapter 2, we discuss the galaxy sample selection and stellar mass completeness, as well as how we select protocluster members given the photometric redshift precision. Our methodology for constructing the SMFs is presented in Section 3, and the results are described in Chapter 4. In Chapter 5 we discuss the implications of our findings, including a comparison with plausibly descendent $1 < z < 1.5$ group SMFs from Reeves et al. (2021).

All magnitudes are presented in the AB magnitude system (Oke, 1974). We used the 'vanilla' ΛCDM cosmology model ($\Omega_m = 0.3, \Omega_\Lambda = 0.7, \mathrm{H}_0 = 70$ km s^{-1} Mpc^{-1}). Stellar

mass estimates are taken from COSMOS2020, which assumes a Chabrier (2003) inital mass function. We present uncertainties at the 1σ level unless otherwise specified.

Chapter 2

Data

2.1 COSMOS2020 Sample Selection

Our data are taken from the COSMOS2020 catalogue (W22), based on a $izYJHK_s$ detection image. We restrict our analysis to data within the UltraVISTA survey footprint (McCracken et al., 2012) that are not in the bright star HSC-SSP PDR2 mask nor in the bright star Suprime-Cam mask. This region corresponds to ~ 1.278 deg^2 and is flagged in the catalogue as `FLAG_COMBINED == 0`. We also limit our sources to ones with photometry measured by `The Farmer` algorithm. `The Farmer`, henceforth simply `Farmer`, is a software package that uses `The Tractor` (Lang et al., 2016) to model and create a full multi-wavelength catalog. Specifically, we take the photometric redshifts, mass and rest-frame magnitude measurements from the `LePhare` (Arnouts & Ilbert, 2011) in combination with `Farmer`. This is because this combination has been noted to have the best photo-z performance (W22; W23).

This region selection leaves us with a subset of the catalog with 746976 entries. When we restrict this sample to galaxies between $1.8 < z < 2.7$, we are left with 105664 entries. This choice of redshift range is informed by the precision of COSMOS2020 photometric redshifts (see Sec. 2.3) around our protocluster sample ($2 < z < 2.5$; see Sec. 2.4). We then select all objects that are above the 5σ IRAC channel 1 magnitude limit of 26 to ensure reliable stellar mass measurements. This magnitude cut removes 23726 objects, leaving 81938 galaxies. While this is a large cut, W23 note that $\sim 93\%$ of these sources are below our optimistic mass limit and thus will be excluded anyway (see Sec. 2.2). To remove objects with poor photometric redshifts, we restrict our analysis to "good" fits (`lp_chi2_best < 5`), removing another 779 galaxies (0.95%). We also require `lp_zPDF_u68` and `lp_zPDF_l68`,

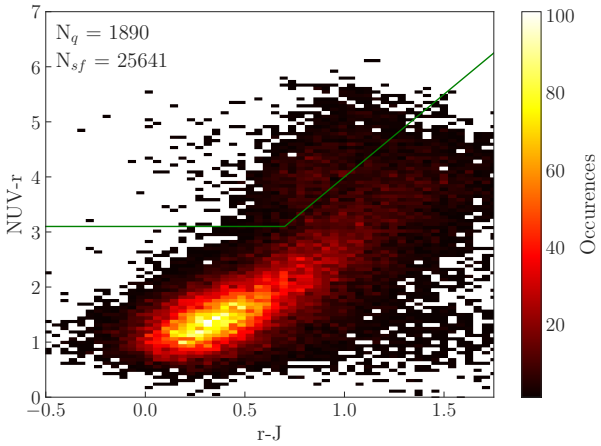

Figure 2.1: We show the NUVrJ colour-colour diagram for all galaxies in our sample between $1.8 < z < 2.7$ above our mass limit (see Sec. 2.2). The green line shows the division between the quiescent and star-forming galaxies (Ilbert et al., 2013), with the quiescent population being above this line and the star forming one below it. We use this definition throughout this analysis. N_q and N_{sf} are the number of quiescent and star-forming galaxies identified by this criterion, respectively.

the upper and lower 68 percentile confidence levels of the photometric redshift respectively, to differ by < 1.0 to ensure that our photometric redshifts are relatively accurate, further removing 1653 galaxies (2.0%) and leaving us with 79506 galaxies in our sample.

Colour-colour diagnostics are effective at separating dusty star-forming galaxies from quiescent ones (Arnouts et al., 2007; Ilbert et al., 2013). We use rest-frame colours provided in the W22 catalogue. In Figure 2.1 we show the (NUV - r) and (r - J) colour distribution for our sample. The use of rest NUV magnitudes in this diagnostic provides more sensitivity to age than the typical UVJ diagrams (Martin et al., 2007; Arnouts et al., 2007). To split the total population into quiescent and star-forming galaxies, we use the definition of Ilbert et al. (2013) where galaxies with rest-frame colours such that $(NUV-r) > 3(r-J)+1$ and $(NUV-r) > 3.1$ (hereby referred to as NUVrJ selection) are considered quiescent. This selection approximates a cut in sSFR $\lesssim 10^{-11}$ yr^{-1} (Ilbert et al., 2013; Davidzon et al., 2017), and is shown as the green line in Fig. 2.1. Note that at this redshift, the bimodality in colour distribution is still apparent, though the two populations are not completely disjoint. We also caution that galaxies with very recently terminated star formation may still be classified as star-forming using the NUVrJ method (e.g. McConachie et al., 2022).

2.2 Mass Completeness Limit

To find the mass completeness of the subset of COSMOS data used in this analysis, we take a similar approach to W23, as originally presented in Pozzetti et al. (2010). W23 use the `IRAC_CH1` limiting magnitude to estimate the mass completeness, as described further below. This will overestimate the completeness, because red objects detected in `IRAC_CH1` may be missed in the detection image (Davidzon et al., 2017, W22). Indeed, a comparison with the deeper CANDELS (The Cosmic Assembly Near-infrared Deep Extragalactic Legacy Survey; Grogin et al., 2011; Koekemoer et al., 2011) catalogue shows that, at the determined 95% mass limit, only 75% of CANDELS sources are recovered. A more conservative choice is to use the K_s band limit; this will underestimate the completeness because the deep Subaru/HSC photometry will allow the detection of galaxies below that limit. We therefore take the approach of showing our results relative to both mass limits. Although `IRAC_CH1` is a significantly better tracer of stellar mass for $z \gtrsim 2.5$, at the redshifts of interest here K_s is still acceptable.

Following W23, we bin the galaxies in redshift and identify a cutoff magnitude $m_{\rm cutoff}$ that corresponds to the $30^{\rm th}$ percentile of magnitudes in that bin for each band. We then consider all galaxies with a magnitude fainter than $m_{\rm cutoff}$ and re-scale their masses so that their apparent magnitude in a given band matches the limiting magnitude:

$$\log_{10}\left(\frac{M_{\rm rescale}}{M_\odot}\right) = \log_{10}\left(\frac{M_*}{M_\odot}\right) + 0.4(m - m_{\rm lim}), \tag{2.1}$$

Where m is the magnitude in a given band, and $m_{\rm lim}$ is the limiting magnitude in that band (26.0 for `IRAC_CH1` and 25.7 for `UVISTA_Ks_MAG` (Weaver et al., 2022b, W22)). We then take our limiting mass $M_{\rm lim}$ to be the $95^{\rm th}$ percentile of the re-scaled mass distribution in each bin and fit a polynomial to these $M_{\rm lim}$ as a function of redshift. We do this for the total, star-forming and quiescent populations.

The mass completeness of our sample compared to the one presented in W23 is shown in Fig. 2.2. Given that our analysis is restricted to protoclusters between $2 < z < 2.5$ and the furthest associated galaxies should be at roughly $z = 2.7$ (see section 2.3), we conservatively restrict our analysis to galaxies above the mass limit at this redshift. Using this, we obtain a `IRAC_CH1`-based mass completeness limit of $\log_{10} M_{\rm lim}/M_\odot = 9.1$ for the total population, 9.5 for the quiescent population, and 9.1 for the star-forming population.

We take our aforementioned mass completeness values as our optimistic mass completeness limit. We follow the same procedure in the K_s magnitude band (which has a limiting

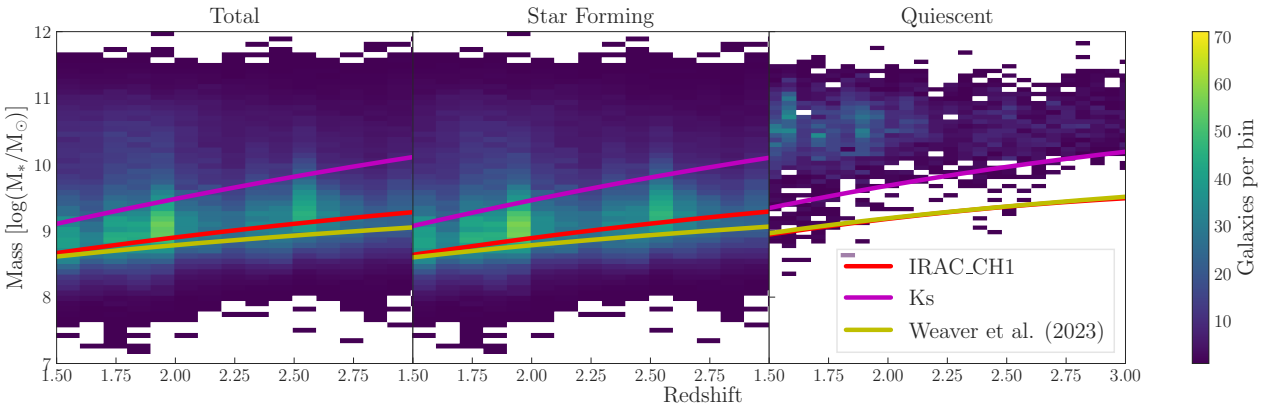

Figure 2.2: Stellar mass completeness as a function of redshift for our COSMOS2020 subsample in the left panel, with the sample restricted to star-forming and quiescent galaxies in the middle and right panels, respectively. The colour indicates the number of galaxies in each bin of redshift and stellar mass. The mass completeness is determined following W23, based on either the `IRAC_CH1` magnitude limit (optimistic, shown as the red line) or the K_s magnitude limit (conservative, shown as the magenta line), as described in the text. This is compared with the `IRAC_CH1`-based completeness from W23, shown as the yellow-green line. At the furthest redshift considered in this analysis ($z \sim 2.7$), we are complete down to $\sim 10^{10}\mathrm{M}_{\odot}$ in our most conservative limit, and complete down to $\sim 10^{9.5} M_{\odot}$ in our optimistic limit.

Population	$\log_{10}(M_{\rm lim}/M_\odot)$ at $z = 2.7$		$\log_{10}(M_{\rm lim}/M_\odot)$ fit	
	IRAC_CH1	K_s	IRAC_CH1	K_s
Quiescent	9.5	10.0	$-0.11(1+z)^2 + 1.08(1+z) + 6.93$	$-0.11(1+z)^2 + 1.28(1+z) + 6.83$
Star-Forming	9.1	9.9	$-0.07(1+z)^2 + 0.89(1+z) + 6.85$	$-0.09(1+z)^2 + 1.27(1+z) + 6.46$
Total	9.1	9.9	$-0.06(1+z)^2 + 0.80(1+z) + 7.04$	$-0.08(1+z)^2 + 1.19(1+z) + 6.63$

Table 2.1: Stellar mass limits for each population. We first show both the IRAC_CH1 -based and K_s -based mass limits, evaluated at $z = 2.7$ for each population. We also show each mass limit as a polynomial function of redshift.

magnitude of 25.7) to give conservative mass completeness limits of $\log_{10}(M_{\rm lim}/M_\odot) = 9.9$ for both the total and star-forming populations, and 10.0 for the quiescent population. We summarize our mass limits, both IRAC_CH1 based and K_s based in Table 2.1. Our final sample for galaxies with $\log_{10}(M_*/M_\odot) > 9.5$, above the optimistic mass completeness limit for quiescent galaxies, consists of 27531 galaxies, of which 1890 are quiescent and 25641 are star-forming.

2.3 Photometric Redshifts

We now consider the uncertainties on the photometric redshifts for the redshift range of interest ($1.8 < z < 2.7$). In the following, we define Δz to be half the difference between the upper and lower 68% confidence limits from the LePhare code as provided by W22. These uncertainties have been shown to represent the scatter between photometric and spectroscopic redshifts well (see W22, Fig 13). Although the outlier fraction becomes large ($\sim 20\%$) at the magnitude limit of the sample, most of these outliers are high redshift ($z_{\rm spec} > 3$) galaxies with $z_{\rm phot} < 1$, and thus do not impact our sample selection. However we caution that spectroscopy at $2 < z < 3$ is very challenging from the ground, particularly for quiescent galaxies, and samples are therefore biased. Therefore the photometric redshift uncertainties at the magnitude limit cannot be considered to be as well characterized as for the rest of the sample.

In Fig. 2.3, we show $\Delta z/(1+z)$ as a function of redshift and mass for galaxies in our sample after the selections described in Section 2.1. The precision of the photometric redshifts do not depend significantly on redshift or mass in this redshift regime. For the redshift range of our sample, $1.8 < z < 2.7$, 95% of all star-forming galaxies have $\Delta z/(1+z) < 0.06$, which corresponds to $\Delta z \approx 0.2$ at $z = 2.25$, the midpoint redshift in this range. When considering quiescent galaxies, 95% of all entries have a $\Delta z/(1+z) < 0.09$, which corresponds to $\Delta z \approx 0.3$ at $z = 2.25$.

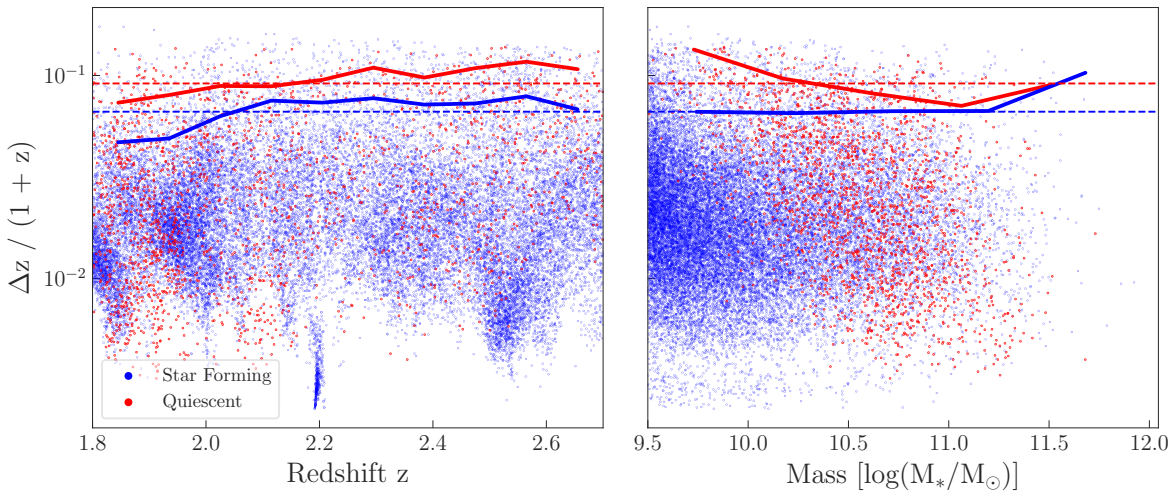

Figure 2.3: *Left:* The dependence of $\Delta z/(1+z)$ as a function of redshift and for galaxies in COSMOS2020 between $1.8 < z < 2.7$ where Δz is defined to be the mean distance between the upper 1σ limit and the lower one. The dashed lines are the overall upper 2σ of the identified sample over the whole redshift range shown, while the solid lines are the upper 2σ limit in bins of redshift. We note a slight increase in Δz as a function of redshift. At the midpoint of $z = 2.25$ the upper 2σ value is $\Delta z \approx 0.2$ for star-forming galaxies and 0.3 for quiescent ones. *Right:* Similar, but for $\Delta z/(1+z)$ as a function of stellar mass. There is a modest decrease with increasing mass, for quiescent galaxies.

2.4 Cluster Membership

While many $z > 2$ protocluster candidates have been identified in the literature, in general it is not possible to know for certain whether these are true protoclusters in the sense that they will evolve into massive ($> 10^{14}$ $M_\odot$) virialized structures by $z = 0$. Recently, Ata et al. (2022) analysed constrained N-body (dark matter only) simulations of the COSMOS density field, with initial fluctuations at $z = 100$ chosen to evolve into the three-dimensional structure within the central square degree of the COSMOS field, as defined by extensive spectroscopic redshifts. From fifty randomly selected realizations of these initial conditions, the simulations are evolved to $z = 0$ to predict the final state of all protocluster candidates in this field. For the present analysis, we consider only those protoclusters that have a high probability (generally $> 80\%$, with one exception) of evolving into massive clusters by $z = 0$ based on their analysis; these are listed in Table 2.2. We start with a summary of each protocluster, though more details can be found in Ata et al. (2022):

ZFOURGE/ZFIRE: This system was first discovered using a near-IR imaging survey with five custom medium-bandwith filters (Spitler et al., 2012), and was then confirmed by a spectroscopic follow up (Yuan et al., 2014). It was measured to have a velocity dispersion of $\sigma = 552 \pm 52$ km s^{-1} (Yuan et al., 2014). In all 50 runs of the constrained simulations, this protocluster was found to evolve into a Coma-like cluster of mass $M_{\rm vir} = (1.2 \pm 0.3) \times 10^{15}\ h^{-1}\ M_\odot$, where $h = \frac{H_0}{100 {\rm kms}^{-1}{\rm Mpc}^{-1}}$.

CC2.2: This protocluster was spectroscopically confirmed by Darvish et al. (2020), following up a large relative overdensity at this location (Darvish et al., 2017). Darvish et al. (2020) estimates a virial mass of $M_{\rm vir} = (1-2) \times 10^{14} M_\odot$ for this structure at its observed redshift, $z \approx 2.2$. In the constrained simulations, a cluster is found at this location 42 out of 50 times, with an associated mass of $M_{\rm vir} = (4.2 \pm 1.9) \times 10^{14}\ h^{-1}\ M_\odot$ by $z = 0$.

Hyperion (1-7): The Hyperion protoclusters were individually found by several studies (Lee et al., 2016; Diener et al., 2015; Chiang et al., 2015; Casey et al., 2015; Wang et al., 2016) before a connection between them was made by Cucciati et al. (2018), which found the system had an estimated total mass of $4.8 \times 10^{15} M_\odot$ over a volume of $\sim$ 60 x 60 x 150 cMpc^3 at $z \sim 2.45$. It was originally hypothesized that this collection of seven density peaks will evolve into a super-cluster by $z = 0$, with the various peaks virializing by redshift $z \sim 0.8-1.6$ (Cucciati et al., 2018). However, the

constrained simulations show that by $z = 0$, four virialized clusters emerge and form a filamentary group of clusters with a total mass of $M_{\rm vir} = (2.5 \pm 0.5) \times 10^{15}\ h^{-1}\ {\rm M}_{\odot}$ spanning $(65 \pm 10)\ h^{-1}$ Mpc. This projected structure is expected to be similar in spatial extent and mass to the Coma/A1367 filament in the local universe (Fontanelli, 1984).

COSTCO Protoclusters: The COnstrained Simulations of The COsmos field (COSTCO) protoclusters are a set of protoclusters found purely through the constrained simulations suite presented in Ata et al. (2022). While they do not have strong overdensities throughout $2 < z < 2.52$, they are extended structures that collapse into Virgo-like clusters ($\sim 10^{14.5}$ M$_{\odot}$) by $z = 0$. COSTCO J100026.4+020940 has previously been identified as an overdensity (Lee et al., 2016). Recently, Dong et al. (2023) noted that the large-scale gas associated with this protocluster has been heated far higher than expected. COSTCO J095945.1+020528 is found to collapse into a cluster only 27 out of 50 times, though in 40 of those simulations it still results in a substantial overdensity at $z = 0$. COSTCO J095945.1+020528 is just south of Hyperion and might become a substructure of it. Tidal disruptions by Hyperion may be the reason why this does not collapse into an independent virialized structure in all cases (Ata et al., 2022).

We identify candidate cluster members by selecting all galaxies within a projected radius dR and a photometric redshift range dz. For sufficiently large dR, these volumes for neighbouring clusters will partially overlap. Since the dz must be large enough to accommodate the significant photometric redshift uncertainties, the volume will be much larger than the physical volume occupied by the cluster, and will include many non-cluster members. These must be corrected statistically, which requires an accurate volume calculation. This is done using a Monte Carlo approach. We take a 'box' of Cartesian space surrounding the clusters, and uniformly populate it with 10^7 points. We first remove all the points outside the UltraVISTA rectangle (McCracken et al., 2012), or in masked regions. We then take the fraction of points inside protocluster cylinders and multiply it by the volume of the box to measure the volume of the protoclusters. For example, for our fiducial cluster volume (see Table 4.1) which has properties $dR = 1$ Mpc and $dz = 0.2$, there are ~ 7750 points inside the protocluster volume. This gives us a volume of $\sim$ 192,000 $\pm$ 2,200 Mpc^3 assuming a Poisson counting error. This precision of ~ 1 % is sufficient that it does not dominate our error budget.

Protocluster Candidate	**RA [deg]**	**Dec [deg]**	**Redshift**	**Projected $z = 0$ Mass**
ZFOURGE/ZFIRE	150.094	2.251	2.095	$(1.2 \pm 0.3) \times 10^{15}\ h^{-1}\ \mathrm{M}_{\odot}$
CC2.2	150.197	2.003	2.232	$(4.2 \pm 1.9) \times 10^{14}\ h^{-1}\ \mathrm{M}_{\odot}$
Hyperion 1	150.093	2.404	2.468	
Hyperion 2	149.976	2.112	2.426	
Hyperion 3	149.999	2.253	2.444	
Hyperion 4	150.255	2.342	2.469	$(2.5 \pm 0.5) \times 10^{15}\ h^{-1}\ \mathrm{M}_{\odot}$
Hyperion 5	150.229	2.338	2.507	
Hyperion 6	150.331	2.242	2.492	
Hyperion 7	149.958	2.218	2.423	
COSTCO J100026.4	150.110	2.161	2.298	$(4.6 \pm 2.2) \times 10^{14}\ h^{-1}\ \mathrm{M}_{\odot}$
COSTCO J095924.0	149.871	2.229	2.047	$(6.1 \pm 2.5) \times 10^{14}\ h^{-1}\ \mathrm{M}_{\odot}$
COSTCO J100031.0	150.129	2.275	2.160	$(5.3 \pm 2.6) \times 10^{14}\ h^{-1}\ \mathrm{M}_{\odot}$
COSTCO J095849.4	149.706	2.024	2.391	$(6.6 \pm 2.3) \times 10^{14}\ h^{-1}\ \mathrm{M}_{\odot}$
COSTCO J095945.1	149.938	2.091	2.283	$(4.3 \pm 2.4) \times 10^{14}\ h^{-1}\ \mathrm{M}_{\odot}$

Table 2.2: A revised version of Table 1 from Ata et al. (2022), providing a list of successful protocluster candidates in the COSMOS2020 field. Each candidate was identified in constrained simulations in the COSMOS field as the location of an overdensity that is likely ($> 50\%$) to evolve into a protocluster (Ata et al., 2022).

Chapter 3

Stellar Mass Functions

3.1 Methodology

To determine the observed number densities, we bin our data by mass and weight each bin by dividing the count by bin size and volume corresponding to the region in question. We take the uncertainty of this to be simply the square root of each count for the respective bins divided by the associated volume.

To fit the unbinned data above the stellar mass limit, we closely follow the Parametric Maximum-Likelihood method (Sandage et al., 1979). We will fit our data with a double (Schechter, 1976) function, as defined in Baldry et al. (2008), in terms of $\mathcal{M} = \log_{10}(M_*/\mathrm{M}_\odot)$:

$$\phi(\mathcal{M}) = \ln(10) \cdot \exp(-10^{(\mathcal{M}-\mathcal{M}^*)}) \cdot 10^{(\mathcal{M}-\mathcal{M}^*)} \cdot \left[\phi_1^* \cdot 10^{(\mathcal{M}-\mathcal{M}^*)\alpha_1} + \phi_2^* \cdot 10^{(\mathcal{M}-\mathcal{M}^*)\alpha_2}\right] \quad (3.1)$$

where $\phi(\mathcal{M})$ is the number of galaxies per Mpc^3 per dex and $\mathcal{M}^* = \log(M^*/\mathrm{M}_\odot)$ is the characteristic mass. The parameters α_1 and α_2 are the high- and low-mass slopes, respectively, with corresponding normalizations ϕ_1^* and ϕ_2^*. This is effectively adding together two Schechter functions with the same $\mathcal{M}^*$. We then assign a probability to each galaxy, as first presented in Oegerle et al. (1986) and Malumuth & Kriss (1986):

$$p_i \equiv p(\mathcal{M}_i) = \frac{\phi(\mathcal{M}_i)}{\int_{\mathcal{M}_{\mathrm{lim}}}^{\infty} \phi(\mathcal{M}) d\mathcal{M}}. \quad (3.2)$$

The likelihood of any given model is defined as the sum of the logarithms of the individual probabilities for each galaxy considered. We determine the parameters $\mathcal{M}^*$, α_1, α_2 and the ratio ϕ_2^*/ϕ_1^* via an MCMC chain. The overall normalization ϕ_1^* is set by forcing the integral of the function above the mass limit to equal the number density of galaxies in the sample. We set our uniform priors to be $\alpha_1 \subseteq$ [-3, 1.5], $\alpha_2 \subseteq$ [-3, -1], $\mathcal{M}^* \subseteq$ [9.5, 12] and ϕ_2^*/ϕ_1^* $\subseteq$ [0, 0.5]. While these priors for α_1 and $\mathcal{M}^*$ are broad and uninformed, the choice of α_2 and ϕ_2^*/ϕ_1^* are specifically motivated to ensure the second component corresponds to any low mass upturn, rather than other possible deviations from a single Schechter function at high mass.

To measure the protocluster SMFs, we measure the SMF in a volume centered on the protoclusters (see Section 4.1). However, as described in Section 4.1, this region is heavily contaminated with field galaxies. To accommodate this, we adjust Equation 3.1:

$$\phi(\mathcal{M}) = \phi_f(\mathcal{M}) + \phi_c(\mathcal{M}), \tag{3.3}$$

where the f and c subscripts are for the field and cluster contributions to the protocluster volume respectively. Both $\phi_f(\mathcal{M})$ and $\phi_c(\mathcal{M})$ are double Schechter functions as in Equation 3.1. We measure ϕ_f for the full field sample (see next section). We then can measure ϕ_c by fitting for Equation 3.3, determining the parameters $\mathcal{M}_c^*$, $\alpha_{1,c}$, $\alpha_{2,c}$ and the ratios $\phi_{2,c}^*/\phi_{1,c}^*$ and $\phi_{1,f}^*/\phi_{1,c}^*$. We then determine $\phi_{1,c}^*$ in the same way we set ϕ_1^*.

This allows us to determine intrinsic protocluster SMF to each (unbinned) population. We also consider the binned data for each population, measured by subtracting the field component in each bin. This is described further in Section 4.2.

3.2 Field Stellar Mass Function and Comparison to Literature

In Fig. 3.1, we show the derived field SMFs observed in our subsample of the COSMOS2020 survey at $2 < z < 2.5$. This definition of the 'field' is simply everything in our sample, which includes both low- and high-density regions. We recover closely the result presented in W22, as expected since we are using the same catalogue. This also agrees reasonably well with the total SMFs presented in Muzzin et al. (2013), McLeod et al. (2021) and Santini et al. (2022) at a similar redshift. Our results show some sensitivity to the redshift range of the field sample, which has been chosen to correspond well to the redshift distribution of our protocluster sample, as described in Appendix A.1.

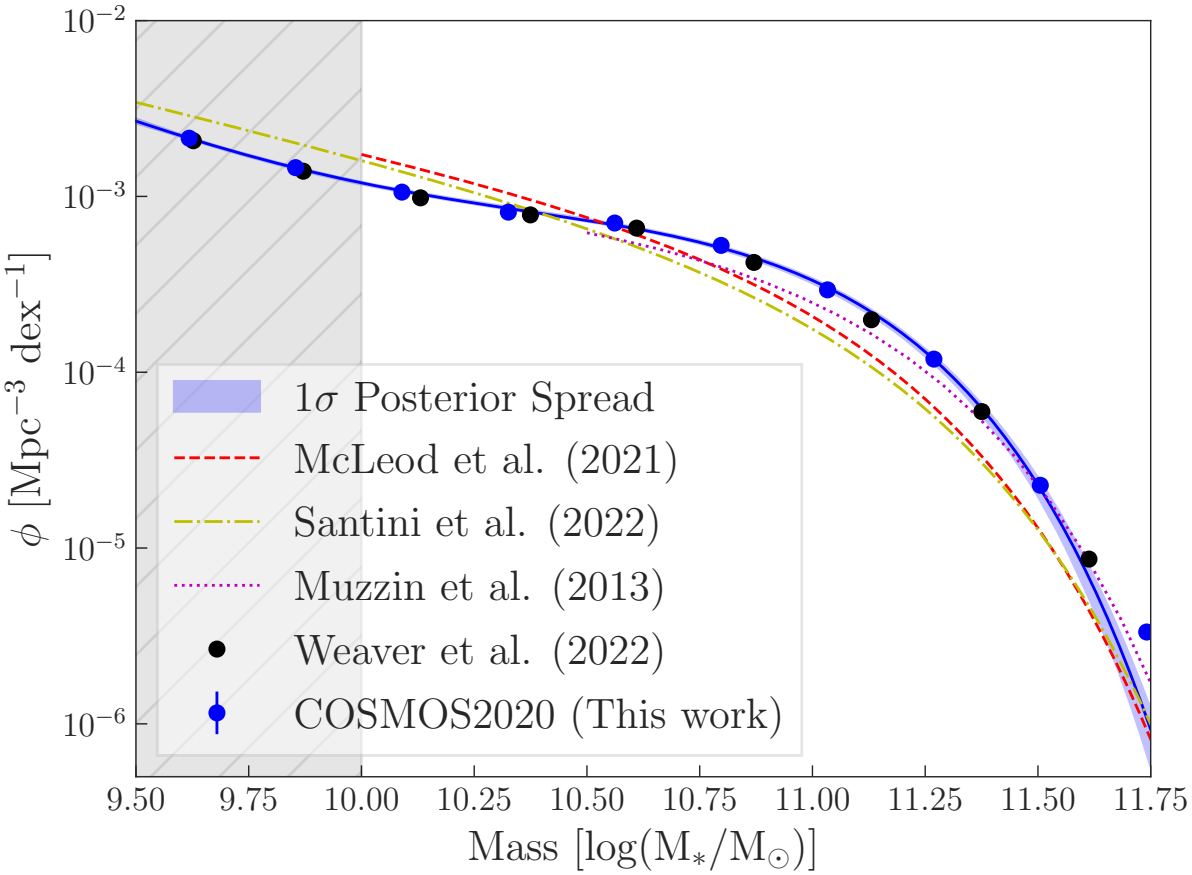

Figure 3.1: We compare the total field SMF at $2 < z < 2.5$ (solid blue line) with measurements from McLeod et al. (2021), Santini et al. (2022), Muzzin et al. (2013) and W23. The results are generally consistent with one another, though there is some variation at the high-mass end. Note there is a small difference in redshift ranges considered, as McLeod et al. (2021) and Santini et al. (2022) are presented for data between $2.25 < z < 2.75$, while Muzzin et al. (2013), W23 and this work are between $2 < z < 2.5$. See Appendix A.2 for a presentation using different redshift bins. The hatched region represents the mass range between our conservative and optimistic mass completeness limits, as discussed in Section 2.2.

We make the same comparison for the quiescent population in Fig. 3.2. While our results are in good agreement with Muzzin et al. (2013) and W23, both McLeod et al. (2021) and Santini et al. (2022) find significantly larger numbers of quiescent galaxies, especially at low stellar masses. Although the redshift ranges do not match exactly, we show in Appendix A.2, Figure A.3, that this does not account for the difference. Differences in the definition of quiescent galaxies are also unlikely to be the explanation. While Santini et al. (2022) and McLeod et al. (2021) use UVJ colours, rather than the NUVrJ selection that we adopt, we show in Figures A.3 & A.4 that this choice does not make a significant difference to the quiescent SMF that we derive (see also Gould et al., 2023). Furthermore, Muzzin et al. (2013) also use a UVJ definition, and their result is similar to ours. Cosmic variance is estimated to account for an uncertainty of only $\sim 20\%$ for the Santini et al. (2022) and McLeod et al. (2021) samples, which is small relative to the $\gtrsim 70$ per cent difference between SMFs. We have checked, using three independent samples of ~ 1000 arcmin^2 (corresponding to the survey area in Santini et al., 2022) within our sample of COSMOS data, that the cosmic variance for the quiescent population is not significantly different than that of the total over most of the mass range. It is possible that the difference lies in the stellar mass or redshift estimates, though all studies use similar methods (e.g. parametric star formation histories, dust law, etc.). Thus, the larger population of quiescent galaxies in McLeod et al. (2021) and Santini et al. (2022) remains unexplained. If it is due to an incompleteness in COSMOS2020, we would expect that to affect our target protocluster volumes (which are only modestly overdense, see Section 4.1) similarly to the general field, in which case any impact on our conclusions based on the comparison of these samples will be small.

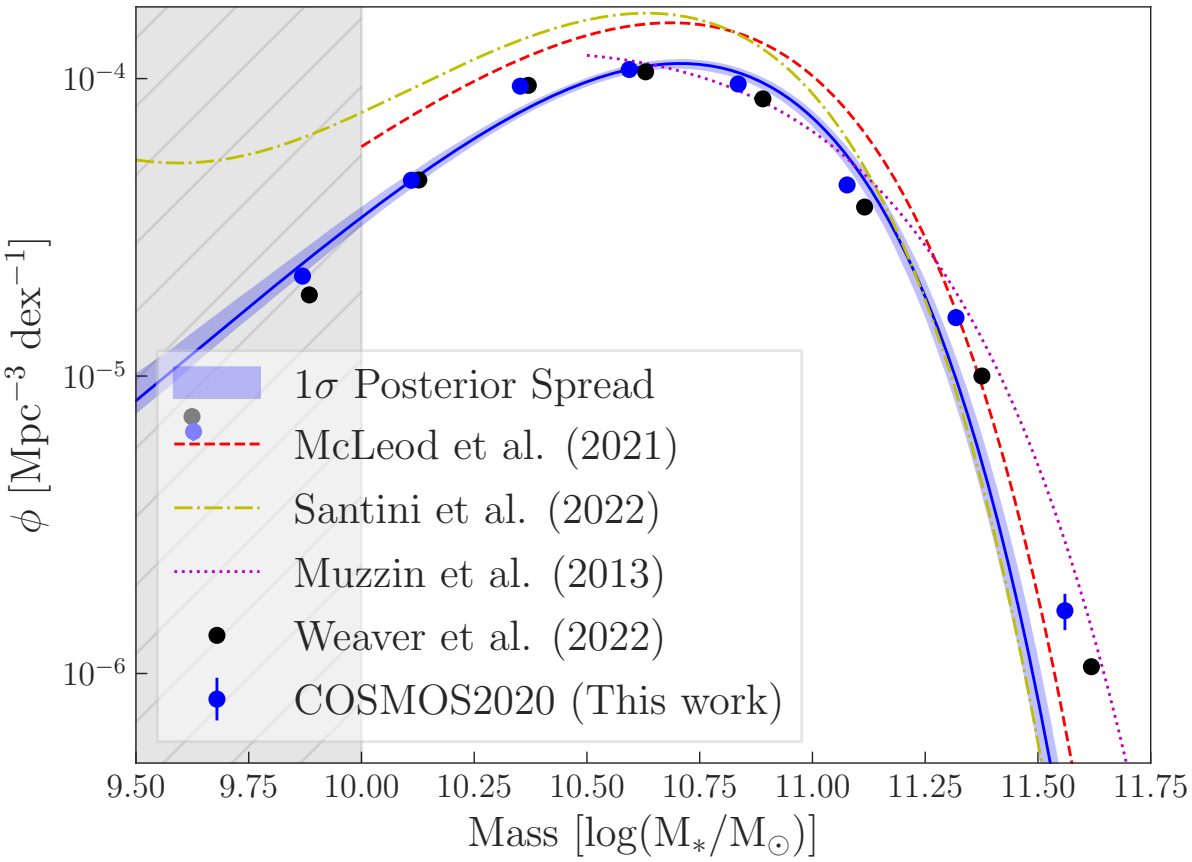

Figure 3.2: We compare the quiescent field galaxy SMF at $2 < z < 2.5$ (solid blue line) for our selected sample with those from W23, McLeod et al. (2021), Santini et al. (2022) and Muzzin et al. (2013). Note that Muzzin et al. (2013) and Santini et al. (2022) use UVJ colours to define quiescent galaxies, while the others (including our work) use NUVrJ. Also, the McLeod et al. (2021) and Santini et al. (2022) results are for a different redshift range of $2.25 < z < 2.75$. See Appendix A.2 for a presentation using different redshift bins and colour selections. The hatched region represents the mass range between our conservative and optimistic mass completeness limits, as discussed in Section 2.2.

Chapter 4

Results

4.1 Protocluster contrast

Due to the large selection volume necessitated by the photometric redshift uncertainties (see Section 2.4), significant field contamination is expected. To quantify this, we measure the contrast of our protocluster sample relative to the field. We calculate the contrast by finding the total number density of galaxies with $\log_{10}(M_*/M_\odot) > 10.5$ in the protocluster selection volume, and subtract the field contribution within that volume from the global SMF. We then divide this quantity by the overall field density to get the relative contrast. In Fig. 4.1 we show how this contrast depends on the choice of dR and dz.

The contrast of our protocluster sample relative to a random field is low, $\lesssim$ 80 per cent. The physical overdensities are likely much higher. For example, if we assume that the protocluster galaxies are contained in a sphere of radius dR = 1Mpc, this contrast corresponds to a physical overdensity of $\sim$1600. While this is very high, this is likely due to the fact that protoclusters are very extended structures, and extend to 10-30 cMpc (Chiang et al., 2013, 2017). The overdensity is likely extended over this amount, rather than contained within a sphere with a radius of 1 Mpc, bringing the physical overdensity to $\sim$ 200.

Our fiducial protocluster selection of $dR = 1$ Mpc and $dz = 0.2$ is physically motivated. The radial extent is chosen to correspond approximately to the virial radius of descendent clusters at $z \sim 1.3$, as discussed further in Section 5.3. The $dz = 0.2$ selection is chosen to correspond to the 95th percentile of photometric redshift error for star-forming galaxies, and is still close to the peak contrast shown in Figure 4.1. In addition to the fiducial

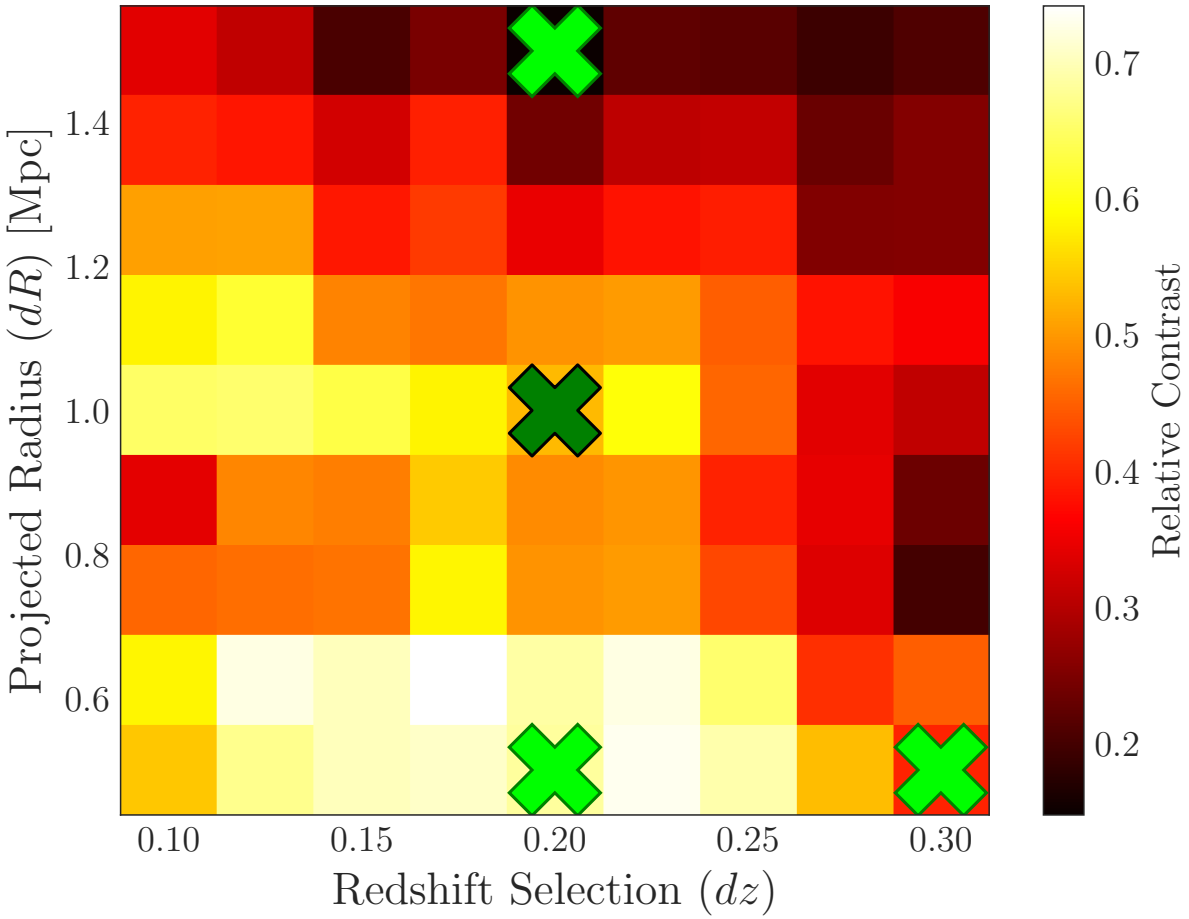

Figure 4.1: The relative contrast is shown as a function of cluster radius dR and redshift selection dz, with our selections (see Table 4.1) indicated by the crosses. Our fiducial sample at $dR = 1$ Mpc and $dz = 0.2$ has a contrast of ~ 50 per cent, and is indicated by the darker cross. A higher contrast is found at smaller dR and dz, at the expense of a less complete sample. Note that dR is in physical units, not comoving.

Selection	Alias	dR, dz	N_q	N_{sf}	N_{tot}
A	Fiducial	1.0, 0.2	32	431	463
B	Core	0.5, 0.2	10	118	128
C	Wide	1.5, 0.2	51	833	884
D	Core-Complete	0.5, 0.3	13	162	175

Table 4.1: The number of quiescent, star-forming and total galaxies in each selection of dR and dz. Most of the analysis in this paper is based on the fiducial sample A, as a good balance between completeness and purity. Selected results for the other samples are provided in Appendix B and Table B.1.

sample, we also consider a "Core" sample restricted to $dR = 0.5$ Mpc. The contrast of this sample is higher, at the cost of a greatly reduced sample size (see Table 4.1). At the other extreme, we consider a "Wide" sample with $dR = 1.5$ Mpc. While it is known that protocluster structures can extend to even larger distances (Muldrew et al., 2015; Chiang et al., 2013; Contini et al., 2016), field contamination dominates in such a volume, making a comparable analysis impractical. Finally we consider a "Core-complete" sample with $dR = 0.5$ Mpc and $dz = 0.3$[1]. The larger redshift selection improves the completeness of the sample for quiescent galaxies. The different samples are listed in Table 4.1, together with the number of quiescent and star-forming galaxies, as defined in Section 2.1. The NUVrJ colour distributions of each sample are shown in Appendix B, Figure B.1.

4.2 Protocluster Stellar Mass Functions

In Fig. 4.2, we show the SMFs for our fiducial selection. Both the total and star-forming and quiescent populations show a significant overdensity relative to the average field, for $\log_{10}(M_*/M_\odot) \lesssim 11$. However, while the shape of the star-forming galaxy SMF is similar to that of the field, the SMF for quiescent galaxies in this volume has an overall flatter shape, indicating relatively more low-mass galaxies than observed in the field. Note that here we are showing show the fit for $\phi(\mathcal{M}) = \phi_f(\mathcal{M}) + \phi_c(\mathcal{M})$, as shown in Equation 3.3 and discussed in Section 3.1.

As discussed in Section 3.1, we also measure the intrinsic protocluster SMF, ϕ_c. The results for our fiducial sample are shown in Fig. 4.3, in units of dex^{-1} cluster^{-1} (left, blue axis). Note this normalization is per cluster rather than per unit volume, since the physical

[1]To create this sample, we apply the same cuts described in section 2.1, but draw from $1.7 < z < 2.8$ instead. We still restrict our analysis to $M_* \geq 10^{9.5} M_\odot$.

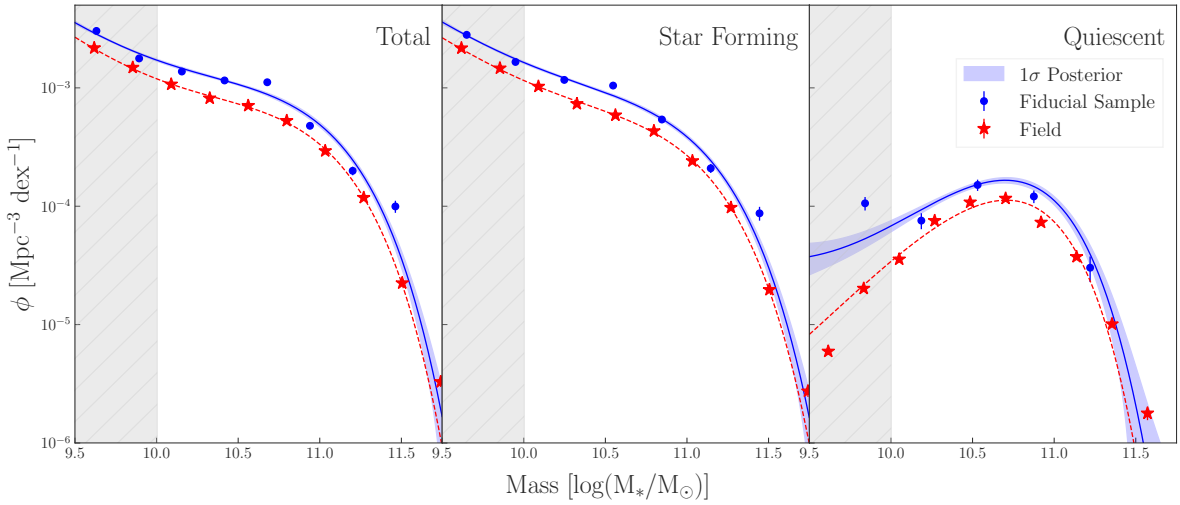

Figure 4.2: The SMFs within the fiducial volume selection A containing the protoclusters, $dR = 1$ Mpc and $dz = 0.2$. The shaded region shows the 1σ uncertainty about the best-fit double Schechter function, which is fit to the unbinned data. The contrast relative to the general field is significant, for the total and star-forming population, at $M_* < 10^{11} M_\odot$. There is evidence for an excess of quiescent galaxies at low stellar masses in the protocluster volumes, relative to the field. The hatched region represents the mass range between our conservative and optimistic mass completeness limits, as discussed in Section 2.2.

volume occupied by the overdensity within our large cylinders is unknown. This is done by multiplying the SMF by the protocluster selection volume and then dividing by the number of clusters. For comparison we plot the corresponding field SMFs, here in units of dex^{-1} Mpc^{-3} (right, red axis). In this representation, the relative normalization of the cluster and field curves has no meaning since the units are not the same. To facilitate comparison of the shapes, we arbitrarily adjust the axis limits. This illustrates how the shape of the dominant star-forming population in the protocluster sample is indistinguishable from that of the field, with a monotonically increasing number of galaxies toward lower stellar mass. However, the shape of the quiescent SMF in the protocluster is qualitatively different from that in the field. While both the field and protocluster SMF peak at $\log_{10}(M_*/M_\odot) \approx 10.75$, the protocluster SMF does not drop off, instead showing signs of an upturn, leading to a relative excess at $\log_{10}(M_*/M_\odot) < 10.5$.

To quantify the significance of the difference in the quiescent galaxy SMFs between the protocluster and the field, we show the confidence intervals of the ratio ϕ_2^*/ϕ_1^* and parameter α_2 for both populations in Fig 4.4. These parameters characterize the low mass upturn in the SMF, where we observe qualitatively different SMFs in the protocluster and field samples. Each distribution is generated from the MCMC chain, measured as described in section 3.1. For display clarity we plot $\log(\phi_2^*/\phi_1^*)$ and $\log(-\alpha_2 - 1)$.

This shows a $\sim 2\sigma$ difference in this parameter combination between the protoclusters and the field. We conclude, therefore, that the difference in shapes at the low mass end is intriguing but not statistically significant.

We show how the intrinsic protocluster SMFs depend on our different selections in Figure 4.5. To allow a clear comparison of the relative shapes on a single plot, we do not show the uncertainty ranges, which are especially large for the two Core samples. The best-fit parameters for all double Schechter function fits are provided in Table B.1. See Appendix B for more details and uncertainty ranges for each sample.

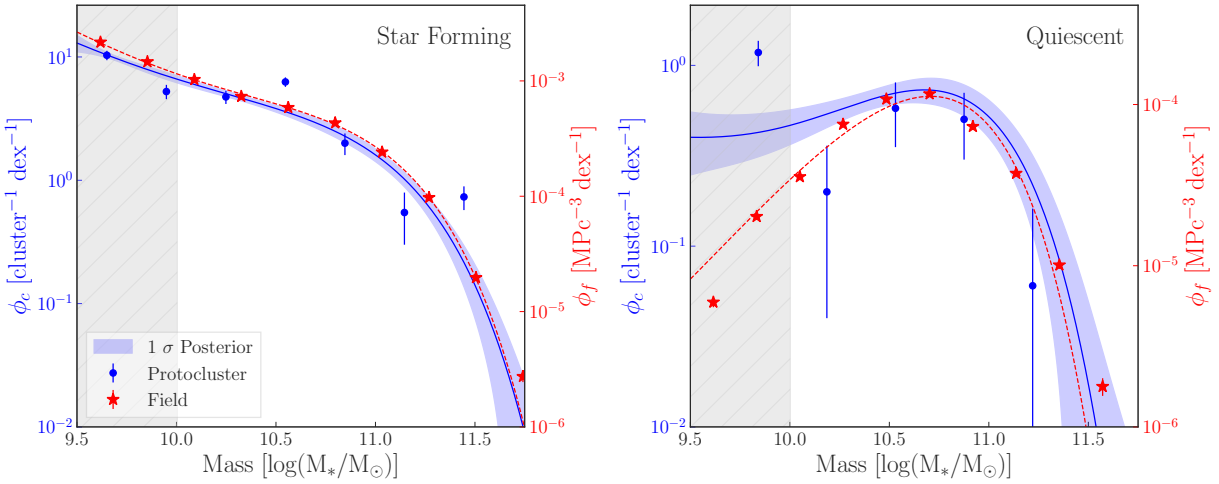

Figure 4.3: The intrinsic SMFs for protocluster galaxies in the fiducial sample (A, Table 4.1) are shown for star-forming (left) and quiescent (right) galaxies. The binned measurements are shown as the blue points, with the blue shaded region representing the difference in the fits to the unbinned data. The SMF of the protocluster is presented in units of dex^{-1}cluster^{-1} (blue, left axis) since the physical volume occupied by the protocluster is unknown. For comparison we show the field SMF in red, and the associated y-axis range (red, on the right side of the panel, in units of dex^{-1}Mpc^{-3}) has been chosen to facilitate comparison of the shapes of the two SMFs such that the field and cluster align near M^*. The shape of the SMFs of the star-forming population matches the shape of the field SMF well, given the uncertainties. However, the quiescent galaxy SMF has a qualitatively different shape from the field. While the number of quiescent galaxies in the field decreases monotonically towards lower masses, in the protocluster an upturn is seen, leading to a relative excess of quiescent galaxies at low mass. Similar plots for the other volume selections of Table 4.1 are shown in Appendix B. The grey hatched region represents the mass range between our conservative and optimistic mass completeness limits, as discussed in Section 2.2.

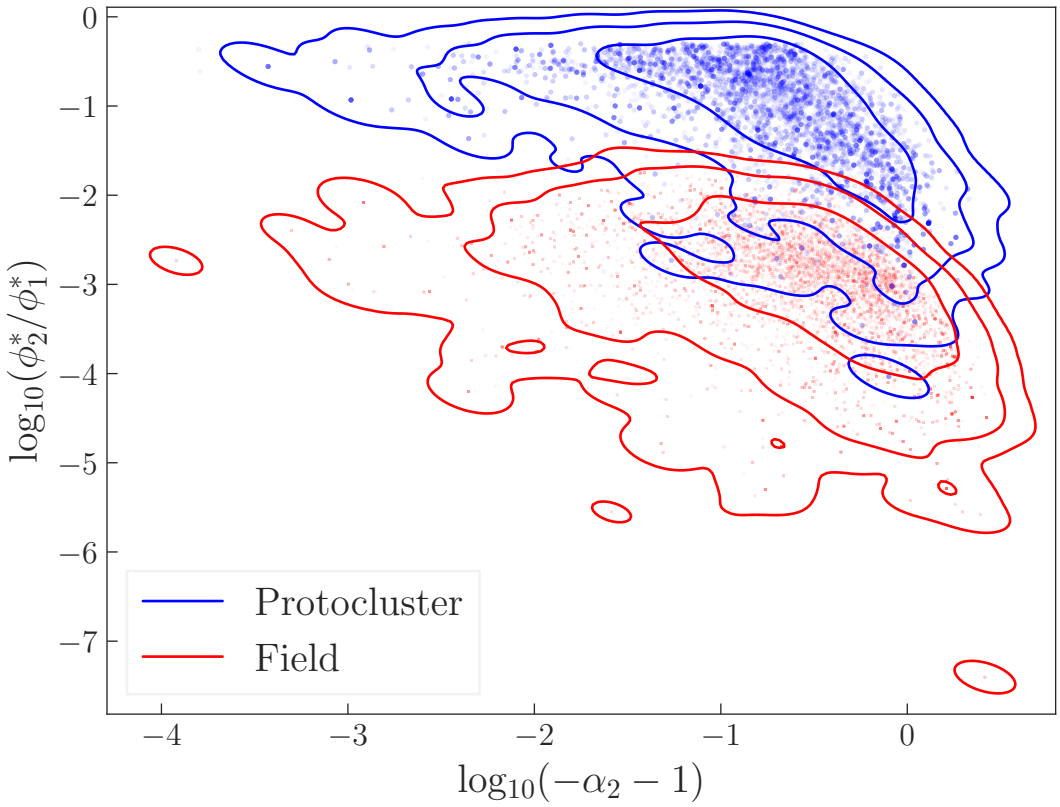

Figure 4.4: The distribution of the log of the ratio ϕ_2^*/ϕ_1^* and parameter $\log(-\alpha_2 - 1)$ for both the protocluster (blue) and the field (red) quiescent populations. The curves show the 1, 2 and 3σ contour levels. This parameter combination in the protocluster differs from that of the field at the $\sim 2\sigma$ level.

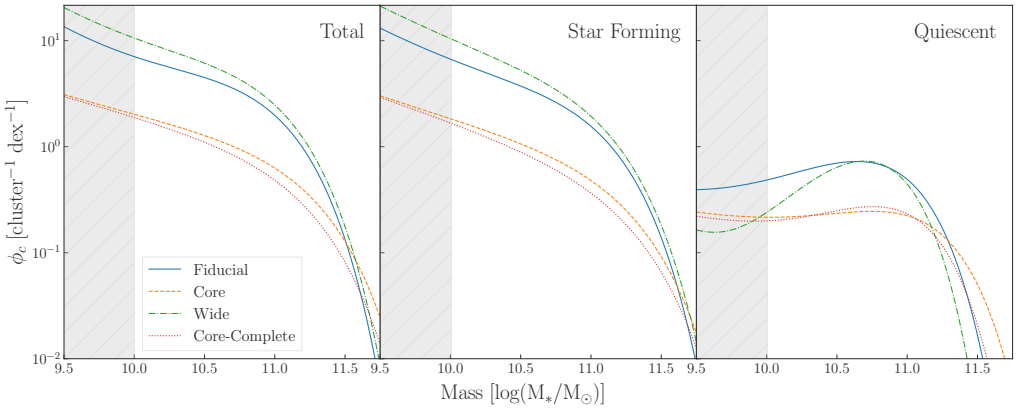

Figure 4.5: The intrinsic protocluster SMFs for each selection volume (Table 4.1). To clearly show the qualitative differences between volume selections, we omit the uncertainty ranges on these figures. The hatched region represents the mass range between our conservative and optimistic mass completeness limits, as discussed in Section 2.2. Individual results for each selection are shown in Appendix B.

Chapter 5

Discussion

5.1 Excess of Low-Mass Quiescent Galaxies

Figures 4.2 and 4.3 show a moderately significant excess of low-mass quiescent galaxies within the protocluster regions. To explore this further, in Figure 5.1 we show the quiescent fraction for our fiducial protocluster sample (dR, dz = 1 Mpc, 0.2), after field subtraction. The fraction is generally quite low, with a 1σ upper limit of ≈ 0.15 for stellar masses with $\log_{10}(M_*/M_\odot) < 10.75$. For most of the stellar mass range, and certainly for $\log_{10}(M_*/M_\odot) > 10.25$, the field and protocluster population have quiescent fractions that are fully consistent with one another, within the substantial 1σ uncertainties. At lower masses we find evidence for a small excess in quiescent fraction, though the statistical significance is not high enough to make strong claims, and larger samples will be required to confirm this. Almost all of these low-mass quiescent galaxies are from the ZFOURGE/ZFIRE protocluster (see Figure B.5), which is the most massive protocluster in our sample. We note also that the apparent excess is in the mass regime where the sample may suffer some incompleteness, though we would expect this incompleteness to affect the protocluster and field samples similarly.

5.2 Comparison with other protocluster literature

As we discuss further in the following subsection, the lack of a dominant quiescent population in these protoclusters is surprising. This result also contrasts with some recent claims for quiescent populations in protoclusters at a similar redshift. In an analysis of

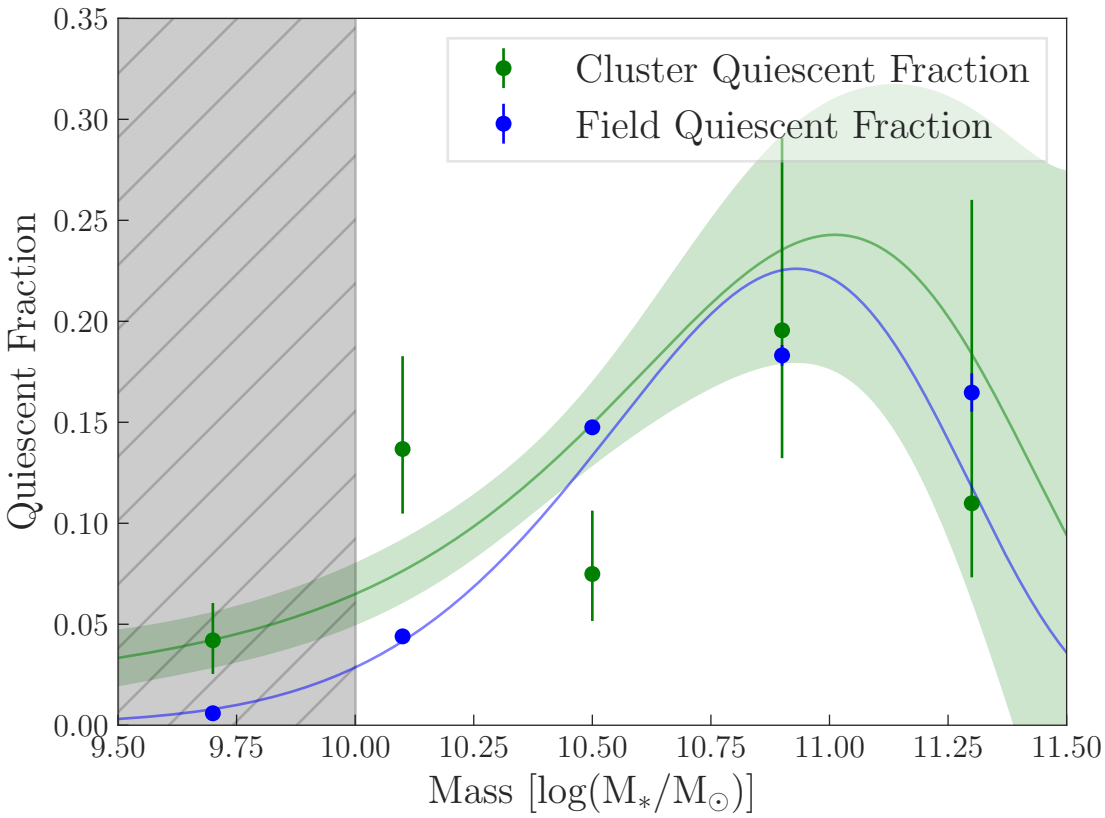

Figure 5.1: The quiescent fraction for galaxies within our fiducial volume selection (A). The field and cluster are statistically indistinguishable for $\log_{10}(M_*/M_\odot) > 10.5$. At lower masses, the cluster sample shows a small excess of quiescent galaxies, though the statistical significance is low. Error bars on the binned data represent the 1σ binomial confidence interval. The green shaded region is derived from the double-Schechter function fits to the unbinned protocluster and field data shown in Figure 4.2.

the cluster QO-1000 at $z = 2.77$, Ito et al. (2023) found 14 quiescent galaxies above mass $\log_{10}(M_*/\mathrm{M}_\odot) > 10.5$, with a number density excess of 4.2σ and a quiescent fraction of 0.34 ± 0.11. Similarly, Ando et al. (2020) analyze 75 protocluster "cores" at $1.5 < z < 3$ in the COSMOS field, using pairs of massive galaxies as tracers. They find a quiescent fraction of 0.17 ± 0.04, three times larger than the field, for $\log(M_*/\mathrm{M}_\odot) > 9$. We note, though, that this sample is dominated by systems at $z < 2$. At somewhat higher redshift $z \approx 3.4$, McConachie et al. (2022) discovered a couple of protoclusters, one of which has a very high quiescent fraction of $0.73^{+0.27}_{-0.17}$ among the most massive galaxies $\log(M_*/\mathrm{M}_\odot) > 11.3$.

To compare with these and other studies, we consider the Quenched Fraction Excess (QFE, van den Bosch et al., 2008; Wetzel et al., 2012; Bahé et al., 2017; van der Burg et al., 2020). This quantity shows the fraction of galaxies that are quenched in the high-density protocluster region, but would expected to be star-forming in the field. This is given by:

$$\mathrm{QFE} = \frac{f_{\mathrm{q,clus}} - f_{\mathrm{q,field}}}{1 - f_{\mathrm{q,field}}}, \tag{5.1}$$

where $f_{\mathrm{q,clus}}$ and $f_{\mathrm{q,field}}$ are the cluster and field quenched fractions, respectively. Since $f_{\mathrm{q,field}}$ is quite small at this redshift, $\lesssim 0.2$, in practice this is not very different from $f_{\mathrm{q,clus}}$.

We calculate the QFE for our sample and compare it to that of other works in the literature in Fig. 5.2. We do this for both our fiducial (blue cross) and core (orange cross) samples, considering all galaxies $M_* > 10^{9.5} M_\odot$. We measure a QFE of $0.03^{+0.04}_{-0.03}$ in the Fiducial sample, and $0.06^{+0.09}_{-0.07}$ for the Core. While low, this is within $\lesssim 2\sigma$ of other high redshift studies such as McConachie et al. (2022), Ito et al. (2023) and Ando et al. (2020).

We noted previously that most of the low-mass quiescent galaxies in our sample come from the most massive system, ZFOURGE/ZFIRE. Considering only this protocluster, using our fiducial parameters $dR, dz = 1, 0.2$, we measure a QFE of $0.13^{+0.12}_{-0.11}$ over the mass range $9.5 \leq \log_{10}(M_*/M_\odot \leq 11.5)$. Over the same mass range, we measure a QFE of $0.00^{+0.04}_{-0.03}$ for the rest of our protoclusters. These two measurements are consistent within 1σ, but hint at a halo-mass dependence that will require larger samples to confirm.

Fig. 5.2 does not present a very clear trend, and the interpretation is complicated by the dependence of QFE on stellar mass, local density or clustercentric radius, and possibly halo mass. There is some indication that a modest quiescent excess is already present in some protoclusters at $2 < z < 3$, and that there is significant evolution toward higher QFE in cluster cores already by $z = 1.6$, only ~ 2 Gyr later. We explore this further in the following section.

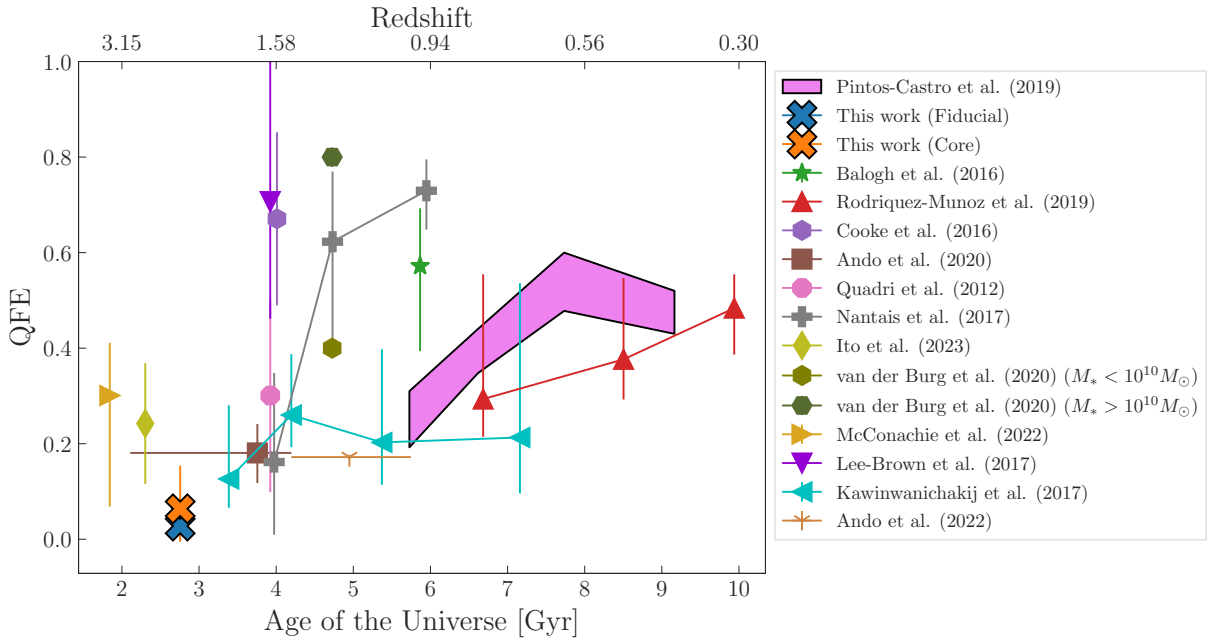

Figure 5.2: The QFE (Equation 5.1) for clusters and protoclusters in our work and the literature as a function of redshift. The mass and cluster-centric radius limits for each work are summarized in Table 5.1. Most are representative of the population with $M_* > 10^{10} M_\odot$, with major exceptions noted in the legend. The blue and orange crosses represent our measurements, for the Fiducial and Core samples, respectively, for $\log_{10} M_*/\mathrm{M}_\odot > 9.5$.

Work	Mass Limit [$\log_{10}(\frac{M_*}{M_\odot})$]	Clustercentric Radius
Ando et al. (2020)	9.5	0.5 Mpc
Ando et al. (2022)	10	0.5 Mpc
Balogh et al. (2016)	10.5	1 Mpc
Cooke et al. (2016)	10.7	$\sim$ 1 Mpc
Ito et al. (2023)	10.3	1 Mpc
Kawinwanichakij et al. (2017)	10.2	
Lee-Brown et al. (2017)	10.2	0.6 Mpc
McConachie et al. (2022)	10.5	2.3 Mpc
Nantais et al. (2017)	10.3	1 Mpc
Pintos-Castro et al. (2019)	10.2	0.4 R/R_{200}
Quadri et al. (2012)	10	0.4 Mpc
Rodríguez-Muñoz et al. (2019)	10	0.2 Mpc
van der Burg et al. (2020)	9.5	1 Mpc

Table 5.1: The mass limits and clustercentric radius for each work shown in Fig. 5.2. We present the clustercentric radius in units of physical Mpc, where available.

5.3 Evolution of the quiescent population in clusters

To compare our results with the $z \sim 1$ descendents of these protoclusters, we note that the average halo mass growth between $z = 2.3$ and $z = 1.3$ is about a factor of 5 (Correa et al., 2015). Assuming the total stellar mass grows by the same factor, we predict a total integrated stellar mass, for galaxies with $\log M_*/M_\odot > 9.5$, of $\log(M_*/M_\odot) \sim 12.1^{+0.05}_{-0.06}$ for the descendent system at $z \sim 1$. From the total stellar mass to halo mass relation at $z \sim 1$ this corresponds to a halo mass of $\log M_{200}/M_\odot \approx 13.7$ (Leauthaud et al., 2012; van der Burg et al., 2014), corresponding to group-scale haloes. We therefore compare with the group sample from Reeves et al. (2021) at $1 < z < 1.5$, which have halo masses between $13.65 \leq \log_{10}(M_{200}/M_\odot) \leq 13.93$. These groups are selected from the COSMOS (UltraVISTA; McCracken et al., 2012; Muzzin et al., 2013) and SXDF (SPLASH-SXDF; Mehta et al., 2018) photometric surveys, and have some spectroscopic coverage by GOGREEN. These systems have a total integrated stellar mass of ~ 12.0 $\log(M_*/M_\odot)$ between $9.5 < \log(M_*/M_\odot) < 11.75$, comparable to the projected mass of our protocluster descendents.

We therefore project our protocluster SMFs to $z = 1.3$ assuming they grow by a factor of 5, by adding sufficient field galaxies to increase the total stellar mass by this factor.

We assume the field is represented by the $1 < z < 1.5$ field SMF that we measure in COSMOS. This ensures that the accreted population evolves identically to the field, with no additional environmentally-driven evolution. Because of this large mass growth, the projected SMF shape is dominated by that of COSMOS $z \sim 1$ field galaxies.

The result is shown in Figure 5.3, compared with both the $1 < z < 1.5$ groups described above, and the more massive GOGREEN-only sample from van der Burg et al. (2020). While our projected SMF has a similar normalization to the group sample, the shapes of the SMFs are different, as the observed $z = 1$ groups have far fewer low-mass galaxies than the projection. This may indicate that a significant amount of merging and disruption occurs among cluster members during this time, as expected (Bahé et al., 2019). An alternate explanation would be that clusters don't grow through the unbiased accretion of field galaxies (Ahad et al., 2023).

When considering just the quiescent population (right panel, Fig.5.3), the predicted number of high-mass quiescent galaxies in our projection is about five times lower than what is observed in the groups at masses $M_* > 10^{10.5}$ $M_\odot$. Additional processes are therefore required to build up massive quiescent galaxies in these groups, with mergers a plausible explanation. However, at lower masses ($M_* < 10^{10.5}$ $M_\odot$), the observed abundance of quiescent galaxies in $z = 1$ groups is consistent with, or even larger than, our projections. This implies that no additional quenching upon infall is required. This is somewhat surprising, as McNab et al. (2021) found from an analysis of post-starburst galaxies that low mass galaxies in massive $z = 1$ clusters have been only quenched recently, upon infall. A plausible explanation of this could be that this is due to a halo mass dependence. The GOGREEN clusters studied in McNab et al. (2021) are about ~ 5 times more massive than the groups in Reeves et al. (2021), on average. Possibly low mass galaxies at this redshift are effectively quenched by environment only when accreted into sufficiently massive structures.

Repeating the above exercise for the massive ZFOURGE/ZFIRE protocluster alone yields a descendent $z = 1.3$ quiescent SMF that is consistent with the GOGREEN/GCLASS observations shown in van der Burg et al. (2020), with little need for additional quenching. The uncertainties are too large to draw any strong conclusions, however, and this must be tested with larger samples of massive protoclusters.

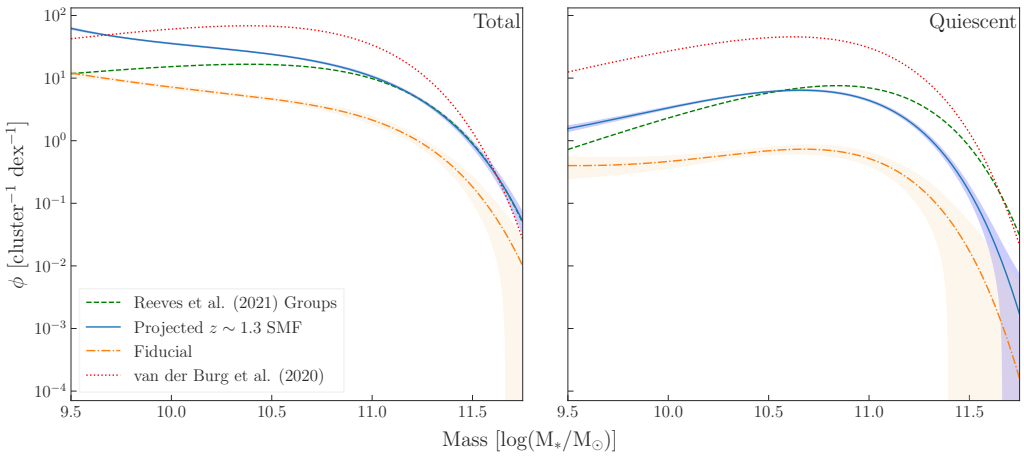

Figure 5.3: The orange curves show our fiducial protocluster SMF, for the total population (left) and quiescent galaxies (right), as presented in Figure 4.3. We project this to $z = 1.3$ by assuming that protoclusters increase in mass by a factor of five through accretion of field galaxies, as described in the text. This projection is shown as the blue curve. This is compared with the observed SMF of Reeves et al. (2021) groups between $1 < z < 1.5$ (green dashed line). We additionally show the observed SMF of the overall GOGREEN cluster sample between $1 < z < 1.5$ (van der Burg et al., 2020) as the red dotted line. *Left*: Our projected total SMF, while having a similar total integrated mass as that of the groups, has a different shape, with significantly more low mass galaxies. This implies significant merging and/or disruption of galaxies, as has been found in lower redshift studies (Rudnick et al., 2012) and simulations (Bahé et al., 2019). *Right*: The shape of the projected quiescent SMF agrees reasonably well with that in the descendent clusters, but with fewer high-mass galaxies. A large number of cluster galaxies at masses above $M_* > 10^{10.5} M_\odot$ must quench star formation in the 2 Gyr between $z = 2.3$ and $z = 1.3$. However, for galaxies with masses below $M_* < 10^{10.5} M_\odot$, no additional quenching upon infall is required.

Chapter 6

Future Work

Most of the protoclusters included in our sample were originally identified based on an overdensity of star-forming galaxies (e.g. Wang et al., 2016). It is possible that this selection is biased against protoclusters with a high fraction of quiescent galaxies. For example, QO-1000 only has a $\sim 1\sigma$ excess of star-forming galaxies, and would never have been identified as a protocluster by just looking at the star-forming population (Ito et al., 2023). Moreover, the COSTCO protoclusters are noted to be mild overdensities at this redshift epoch, and are projected to be relatively low-mass clusters by $z = 0$ (Ata et al., 2022). In contrast, we find evidence that the most massive system in our sample, ZFOURGE/ZFIRE, may have a significantly larger quiescent population than the rest of the sample (see Fig. B.5), though the uncertainties are too large to be definitive. Our results are limited by statistics, and much larger samples are therefore needed. The Euclid deep fields will cover an area > 20 times larger than the COSMOS subset used in this study (Sartoris et al., 2016) and will reach a similar 5σ depth (26 mag) as COSMOS for the Y, J and H filters (Euclid Collaboration et al., 2022). Scaling from our present sample size of 14 protoclusters in a ~ 2 deg^2 region, the resulting uncertainties on the derived protocluster quiescent fraction can be reduced by a factor of $\sim$5. Even better results can be expected from the Nancy Grace Roman Space Telescope (NGRST), which will cover an area that is ~ 40 times larger than the Euclid Deep Fields, to greater depth.

Additionally, at these high-redshifts where protoclusters lie, better photometric redshift precision is important to reduce line-of-sight uncertainties. The upcoming COSMOS-Web catalogues will help with this, as they are expected to be much deeper, reaching 5σ depths of 27.5-28.2 magnitudes in the four NIRCam filters used, spanning ~ 0.54 deg^2 (Casey et al., 2023). The Hyperion structure lies in this field, and its fainter members are expected to be mapped for the first time (Casey et al., 2023). Ultimately, however, the largest gains will

be with spectroscopy. A deep slitless prism survey with NGRST covering just 10 square degrees could identify $\sim 15,000$ protocluster galaxies (Rudnick et al., 2023).

Chapter 7

Conclusions

We measure the SMFs for the total, star-forming and quiescent galaxy populations in protoclusters between $2 < z < 2.5$ in the COSMOS field. These are compared with a comparably selected field sample and are estimated to be complete down to a mass limit of $\log(M_{\rm lim}/M_{\odot}) = 9.5$. We use these SMFs to measure the efficiency of environmental quenching in protocluster regions as opposed to the field. Our main findings are:

- On a scale of 1 Mpc we find a significant overdensity of galaxies in fields centred on the protocluster sample. The shape of the protocluster total SMF, and that of the dominant, star-forming population, is consistent with that of the field (Fig. 4.2).
- The shape of the protocluster quiescent SMF is different from the field. It is flatter than the field at low masses, with a relative excess of galaxies $M_* < 10^{10} M_{\odot}$ (Fig. 4.3). This difference is only significant at a $\sim 2\sigma$ level, however (Fig 4.4).
- The fraction of quenched galaxies in our fiducial protocluster selection is indistinguishable from the field above $M_* > 10^{10} M_{\odot}$. However, there is a small but significant excess ($0.08^{+0.03}_{-0.02}$) at lower masses (Fig. 5.1).
- We compare the protoclusters with a sample of groups at $1 < z < 1.5$ from Reeves et al. (2021). The total stellar mass of those groups within 1 Mpc is about a factor ~ 5 larger than in the protoclusters. This is similar to the expected mass growth over this time (Correa et al., 2015). We calculate a projected descendent SMF by assuming the protoclusters grow via accretion of field galaxies to the mass of the group sample, with no additional quenching. The resulting shape of this projected SMF is significantly different from that of the lower redshift sample, with an excess of

galaxies with $M_* \lesssim 10^{11} M_\odot$ (Fig. 5.3, left panel). This may indicate that significant merging and/or disruption of galaxies takes place between $z = 2.3$ and $z = 1.3$.

- To match the observed quiescent SMF in the group sample, the number of massive quiescent galaxies must increase by about a factor ~ 5 beyond what is predicted from the accretion of field galaxies, between $1.3 \lesssim z \lesssim 2.3$ (Fig. 5.3, right panel). However, at low masses ($\mathrm{M}_* < 10^{10.5} \mathrm{M}_\odot$), no additional quenching upon accretion is necessary, and in fact we project even more low-mass galaxies than are observed in (Reeves et al., 2021). This is surprising, as McNab et al. (2021) shows that in the GOGREEN clusters, low-mass galaxies are expected to have quenched more recently than high-mass ones. This can plausibly be explained by the much larger halo mass of the GOGREEN clusters having more of an environmental effect on low mass galaxies.

We conclude that the SMF of galaxies within 1 Mpc of these protoclusters is similar to that of the field, with a small fraction of quiescent galaxies. There is some evidence for a small excess of low-mass ($\log M/M_\odot < 10$) quiescent galaxies relative to the field, though this is of modest significance and may also be impacted by incompleteness. In any case, these are small in number, and most of the quiescent galaxies that dominate rich clusters at $1 < z < 1.5$ must therefore have been quenched later, presumably upon accretion (though see Ahad et al., 2023, for an alternative explanation). The lack of massive, primordially-quenched galaxies is a surprise given the results of some other studies (e.g. McConachie et al., 2022). As we rely on photometric redshifts with statistical background subtraction, the uncertainties for this small sample of 14 protoclusters are large, especially for $M_* > 10^{11.0} M_\odot$. Future studies based on larger samples (e.g. from the Euclid deep fields) and with more precise and accurate redshifts (e.g. from COSMOS-Web) should significantly improve upon these results.

References

Ahad S. L., Muzzin A., Bahé Y. M., Hoekstra H., 2023, arXiv e-prints, p. arXiv:2307.01147

Albrecht A., Steinhardt P. J., 1982, Phys. Rev. Lett., 48, 1220

Ando M., Shimasaku K., Momose R., 2020, , 496, 3169

Ando M., Shimasaku K., Momose R., Ito K., Sawicki M., Shimakawa R., 2022, , 513, 3252

Arnouts S., Ilbert O., 2011, LePHARE: Photometric Analysis for Redshift Estimate, Astrophysics Source Code Library, record ascl:1108.009 (ascl:1108.009)

Arnouts S., et al., 2007, , 476, 137

Ata M., Lee K.-G., Vecchia C. D., Kitaura F.-S., Cucciati O., Lemaux B. C., Kashino D., Müller T., 2022, Nature Astronomy, 6, 857

Bahé Y. M., et al., 2017, , 470, 4186

Bahé Y. M., et al., 2019, , 485, 2287

Baldry I. K., Balogh M. L., Bower R. G., Glazebrook K., Nichol R. C., Bamford S. P., Budavari T., 2006, , 373, 469

Baldry I. K., Glazebrook K., Driver S. P., 2008, , 388, 945

Balogh M. L., Navarro J. F., Morris S. L., 2000, , 540, 113

Balogh M. L., et al., 2016, , 456, 4364

Balogh M. L., et al., 2021, , 500, 358

Baxter D. C., et al., 2022, , 515, 5479

Baxter D. C., et al., 2023, arXiv e-prints, p. arXiv:2306.09404

Belli S., Newman A. B., Ellis R. S., 2019, , 874, 17

Bernardeau F., Colombi S., Gaztañaga E., Scoccimarro R., 2002, , 367, 1

Bertone G., Hooper D., Silk J., 2005, , 405, 279

Bharadwaj S., Bhavsar S. P., Sheth J. V., 2004, , 606, 25

Blanton M. R., Eisenstein D., Hogg D. W., Schlegel D. J., Brinkmann J., 2005, , 629, 143

Bond J. R., Kofman L., Pogosyan D., 1996, , 380, 603

Boselli A., Gavazzi G., 2006, , 118, 517

Boselli A., Fossati M., Sun M., 2022, , 30, 3

Boylan-Kolchin M., Springel V., White S. D. M., Jenkins A., Lemson G., 2009, , 398, 1150

Bull P., et al., 2016, Physics of the Dark Universe, 12, 56

Carroll S. M., 2001, Living Reviews in Relativity, 4, 1

Carroll B. W., Ostlie D. A., 1996, An Introduction to Modern Astrophysics

Carroll S. M., Press W. H., Turner E. L., 1992, , 30, 499

Casey C. M., 2016, , 824, 36

Casey C. M., et al., 2015, , 808, L33

Casey C. M., et al., 2023, , 954, 31

Ceverino D., Klypin A., 2009, , 695, 292

Chabrier G., 2003, , 115, 763

Chiang Y.-K., Overzier R., Gebhardt K., 2013, , 779, 127

Chiang Y.-K., et al., 2015, , 808, 37

Chiang Y.-K., Overzier R. A., Gebhardt K., Henriques B., 2017, , 844, L23

Cole S., Lacey C., 1996, , 281, 716

Contini E., De Lucia G., Hatch N., Borgani S., Kang X., 2016, , 456, 1924

Contreras S., Zehavi I., 2023, , 525, 4257

Cooke E. A., et al., 2016, , 816, 83

Correa C. A., Wyithe J. S. B., Schaye J., Duffy A. R., 2015, , 450, 1514

Cucciati O., et al., 2018, , 619, A49

Darvish B., Mobasher B., Martin D. C., Sobral D., Scoville N., Stroe A., Hemmati S., Kartaltepe J., 2017, , 837, 16

Darvish B., et al., 2020, , 892, 8

Davidzon I., et al., 2017, , 605, A70

Dekel A., Birnboim Y., 2006, , 368, 2

Dekel A., Silk J., 1986, , 303, 39

Dickinson M., Papovich C., Ferguson H. C., Budavári T., 2003, , 587, 25

Diener C., et al., 2015, , 802, 31

Dong C., Lee K.-G., Ata M., Horowitz B., Momose R., 2023, , 945, L28

Dressler A., 1980, , 236, 351

Ebeling H., Stephenson L. N., Edge A. C., 2014, , 781, L40

Einstein A., 1917, Sitzungsberichte der Königlich Preussischen Akademie der Wissenschaften, pp 142–152

Euclid Collaboration et al., 2022, , 658, A126

Fields B. D., 2011, Annual Review of Nuclear and Particle Science, 61, 47

Fontanelli P., 1984, , 138, 85

Friedmann A., 1922, Zeitschrift fur Physik, 10, 377

Geach J. E., et al., 2005, , 363, 1398

Geller M. J., Huchra J. P., 1989, Science, 246, 897

Gilbank D. G., Balogh M. L., 2008, , 385, L116

Girelli G., Pozzetti L., Bolzonella M., Giocoli C., Marulli F., Baldi M., 2020, , 634, A135

Gómez P. L., et al., 2003, , 584, 210

Gott J. Richard I., Jurić M., Schlegel D., Hoyle F., Vogeley M., Tegmark M., Bahcall N., Brinkmann J., 2005, , 624, 463

Gould K. M. L., et al., 2023, , 165, 248

Grogin N. A., et al., 2011, , 197, 35

Gunn J. E., Gott J. Richard I., 1972, , 176, 1

Guth A. H., 1981, Phys. Rev. D, 23, 347

Hopkins P. F., Hernquist L., Cox T. J., Di Matteo T., Robertson B., Springel V., 2006, , 163, 1

Horvath I., Hakkila J., Bagoly Z., 2013, arXiv e-prints, p. arXiv:1311.1104

Ilbert O., et al., 2013, , 556, A55

Ito K., et al., 2023, , 945, L9

Kaiser N., 1986, , 222, 323

Kauffmann G., White S. D. M., Guiderdoni B., 1993, , 264, 201

Kawinwanichakij L., et al., 2017, , 847, 134

Kodama T., Smail I., Nakata F., Okamura S., Bower R. G., 2001, , 562, L9

Koekemoer A. M., et al., 2011, , 197, 36

Kravtsov A. V., Borgani S., 2012, , 50, 353

Lang D., Hogg D. W., Mykytyn D., 2016, The Tractor: Probabilistic astronomical source detection and measurement, Astrophysics Source Code Library, record ascl:1604.008 (ascl:1604.008)

Larson R. B., Tinsley B. M., Caldwell C. N., 1980, , 237, 692

Leauthaud A., et al., 2012, , 744, 159

Lee-Brown D. B., et al., 2017, , 844, 43

Lee K.-G., et al., 2016, , 817, 160

Leja J., Speagle J. S., Johnson B. D., Conroy C., van Dokkum P., Franx M., 2020, , 893, 111

Lewis I., et al., 2002, , 334, 673

Linde A. D., 1982, Physics Letters B, 108, 389

Lovell C. C., Thomas P. A., Wilkins S. M., 2018, , 474, 4612

Malumuth E. M., Kriss G. A., 1986, , 308, 10

Martin D. C., et al., 2007, , 173, 342

McConachie I., et al., 2022, , 926, 37

McCracken H. J., et al., 2012, , 544, A156

McGee S. L., Balogh M. L., Wilman D. J., Bower R. G., Mulchaey J. S., Parker L. C., Oemler A., 2011, , 413, 996

McLeod D. J., McLure R. J., Dunlop J. S., Cullen F., Carnall A. C., Duncan K., 2021, , 503, 4413

McNab K., et al., 2021, , 508, 157

Mehta V., et al., 2018, , 235, 36

Migkas K., Schellenberger G., Reiprich T. H., Pacaud F., Ramos-Ceja M. E., Lovisari L., 2020, , 636, A15

Mihos J. C., Hernquist L., 1994, , 425, L13

Moore B., Katz N., Lake G., Dressler A., Oemler A., 1996, , 379, 613

Moore B., Lake G., Katz N., 1998, , 495, 139

Moore B., Lake G., Quinn T., Stadel J., 1999, , 304, 465

Muldrew S. I., Hatch N. A., Cooke E. A., 2015, , 452, 2528

Muzzin A., et al., 2012, , 746, 188

Muzzin A., et al., 2013, , 777, 18

Muzzin A., et al., 2014, , 796, 65

Nantais J. B., et al., 2017, , 465, L104

Nelson D., et al., 2019, Computational Astrophysics and Cosmology, 6, 2

Newton I., 1687, Philosophiae Naturalis Principia Mathematica., doi:10.3931/e-rara-440.

Oegerle W. R., Hoessel J. G., Ernst R. M., 1986, , 91, 697

Oke J. B., 1974, , 27, 21

Overzier R. A., 2016, , 24, 14

Page L., et al., 2003, , 148, 233

Pan D. C., Vogeley M. S., Hoyle F., Choi Y.-Y., Park C., 2012, , 421, 926

Peebles P. J. E., 1984, , 284, 439

Peebles P. J. E., 2001, , 557, 495

Peebles P. J. E., 2022, Annals of Physics, 447, 169159

Peebles P. J., Ratra B., 2003, Reviews of Modern Physics, 75, 559

Peng Y.-j., et al., 2010, , 721, 193

Perivolaropoulos L., Skara F., 2022, , 95, 101659

Perlmutter S., et al., 1999, , 517, 565

Pillepich A., et al., 2018, , 473, 4077

Pintos-Castro I., Yee H. K. C., Muzzin A., Old L., Wilson G., 2019, , 876, 40

Planck Collaboration et al., 2020, , 641, A6

Poggianti B. M., et al., 2006, , 642, 188

Poggianti B. M., et al., 2017, , 844, 48

Popescu R., et al., 2023, arXiv e-prints, p. arXiv:2308.00745

Pozzetti L., et al., 2010, , 523, A13

Press W. H., Schechter P., 1974, , 187, 425

Quadri R. F., Williams R. J., Franx M., Hildebrandt H., 2012, , 744, 88

Reeves A. M. M., et al., 2021, , 506, 3364

Riess A. G., et al., 1998, , 116, 1009

Roberts I. D., et al., 2021, , 650, A111

Rodríguez-Muñoz L., et al., 2019, , 485, 586

Rubin V. C., Ford W. Kent J., 1970, , 159, 379

Rubin V. C., Ford W. K. J., Thonnard N., 1980, , 238, 471

Rudnick G., et al., 2003, , 599, 847

Rudnick G., et al., 2006, , 650, 624

Rudnick G. H., Tran K.-V., Papovich C., Momcheva I., Willmer C., 2012, , 755, 14

Rudnick G., et al., 2023, arXiv e-prints, p. arXiv:2306.15735

Sandage A., Tammann G. A., Yahil A., 1979, , 232, 352

Santini P., et al., 2022, , 940, 135

Sartoris B., et al., 2016, , 459, 1764

Schechter P., 1976, , 203, 297

Scoville N., et al., 2007, , 172, 1

Secrest N. J., von Hausegger S., Rameez M., Mohayaee R., Sarkar S., Colin J., 2021, , 908, L51

Silk J., Rees M. J., 1998, Quasars and Galaxy Formation (arXiv:astro-ph/9801013)

Smith R. J., et al., 2010, , 408, 1417

Spitler L. R., et al., 2012, , 748, L21

Springel V., Di Matteo T., Hernquist L., 2005, , 620, L79

Starobinsky A. A., 1980, Physics Letters B, 91, 99

Taylor E., Almaini O., Merrifield M., Maltby D., Wild V., Hartley W. G., Rowlands K., 2023, , 522, 2297

Thomas D., Maraston C., Bender R., Mendes de Oliveira C., 2005, , 621, 673

Tully R. B., Courtois H., Hoffman Y., Pomarède D., 2014, , 513, 71

Turner M. S., 2022, Annual Review of Nuclear and Particle Science, 72, 1

Wang T., et al., 2016, , 828, 56

Weaver J. R., et al., 2022a, arXiv e-prints, p. arXiv:2212.02512

Weaver J. R., et al., 2022b, , 258, 11

Webb K., et al., 2020, , 498, 5317

Wechsler R. H., Tinker J. L., 2018, , 56, 435

Werner S. V., Hatch N. A., Muzzin A., van der Burg R. F. J., Balogh M. L., Rudnick G., Wilson G., 2022, , 510, 674

Wetzel A. R., Tinker J. L., Conroy C., 2012, , 424, 232

White S. D. M., Frenk C. S., 1991, , 379, 52

Yang H. Y. K., Reynolds C. S., 2016, , 829, 90

Yuan T., et al., 2014, , 795, L20

Zabludoff A. I., Zaritsky D., Lin H., Tucker D., Hashimoto Y., Shectman S. A., Oemler A., Kirshner R. P., 1996, , 466, 104

Zehavi I., et al., 2005, , 630, 1

Zuhone J., Markevitch M., 2009, in Heinz S., Wilcots E., eds, American Institute of Physics Conference Series Vol. 1201, The Monster's Fiery Breath: Feedback in Galaxies, Groups, and Clusters. pp 383–386 (arXiv:0909.0560), doi:10.1063/1.3293082

Zwicky F., 1933, Helvetica Physica Acta, 6, 110

Zwicky F., 1937, , 86, 217

van den Bosch F. C., Aquino D., Yang X., Mo H. J., Pasquali A., McIntosh D. H., Weinmann S. M., Kang X., 2008, , 387, 79

van der Burg R. F. J., Muzzin A., Hoekstra H., Wilson G., Lidman C., Yee H. K. C., 2014, , 561, A79

van der Burg R. F. J., et al., 2020, , 638, A112

APPENDICES

Appendix A

Field Considerations

A.1 Redshift distribution of the Field

In this work, we define our 'field' to be all objects that match our cut selection (see Section 2.1) between $2 < z < 2.5$. This differs from the range in which our candidate protocluster members are selected, $1.8 < z < 2.7$. The broader range is necessary to accommodate photometric redshift uncertainties (see Section 2.3). The normalization of the field SMF is somewhat sensitive to the redshift range, and we choose the narrower $2 < z < 2.5$ to better match the redshift distribution of the protocluster members. In particular, there are overdense structures at $1.8 < z < 2$ that significantly perturb the field SMF when that range is included.

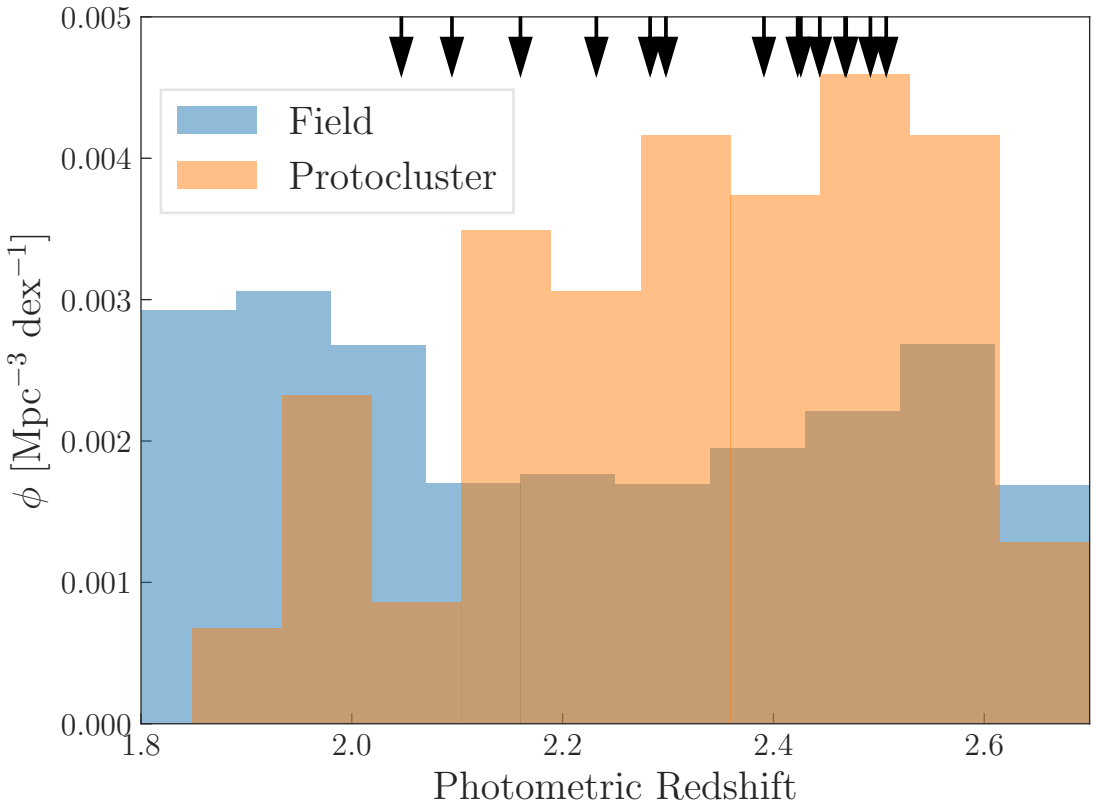

Figure A.1: The distribution of field and protocluster (fiducial selection, Table 4.1) photometric redshifts. Arrows indicate individual protocluster candidate redshifts (Table 2.2). As can be seen, the majority of protocluster galaxies lie in the $2 < z < 2.5$ redshift range, as expected. Selecting a field sample in this same range helps to ensure a similar redshift distribution as the clusters, by avoiding the overdense structures between $1.8 < z < 2$.

A.2 Field Comparison

In Figure 3.1 we compared the total and quiescent SMFs in our field sample to that measured in previous studies. As noted in the text, there are some differences in how our sample is constructed relative to those comparison studies. Here we show the extent to which these differences affect the SMF measurements. First, in Figure A.2 we show the total SMF in three different redshift bins, $0.25 < z < 0.75$, $1.25 < z < 1.75$ and $2.25 < z < 2.75$. The latter bin is different from our default field sample ($2 < z < 2.5$), chosen here to correspond to the binning of McLeod et al. (2021) and Santini et al. (2022). In general, the total SMF agrees well with both those works, as well as that of Muzzin et al. (2013), in all three redshift ranges, for $M_* < 10^{11} M_\odot$. We also show the effect of using our default photometric catalogue, `Farmer`, compared with the `Classic`. The difference is largely negligible, especially at the $z \approx 2$ epoch that is central to this work.

Figure A.3 is similar, but for just the quiescent population. The lower normalization that we observe relative to McLeod et al. (2021) and Santini et al. (2022) persists even when we use the same redshift interval $2.25 < z < 2.75$, and also extends to the lower redshift interval $1.25 < z < 1.75$. We also observe that the choice of catalogue (the default, `Farmer`, compared with the `Classic`) has a significant impact on the quiescent SMF at low stellar masses, as discussed by W22 and W23.

Finally, we consider the impact of selecting quiescent galaxies from a UVJ colour selection, rather than our default NUVrJ. The result is shown in Figure A.4, for the same redshift bins as the previous two figures. Again, the different choice in definition does not remove the discrepancy with McLeod et al. (2021) and Santini et al. (2022).

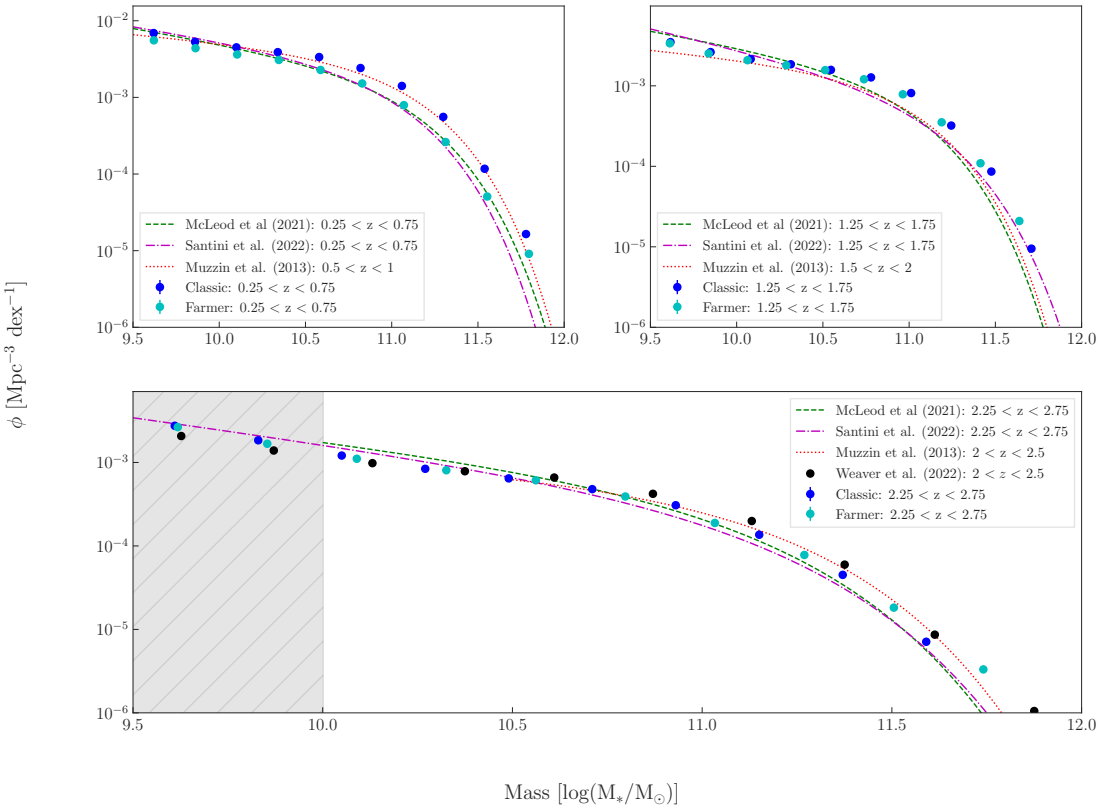

Figure A.2: We show the total SMF of our field sample in three redshift bins, chosen to correspond to those of McLeod et al. (2021) and Santini et al. (2022). There is good agreement for $M_* < 10^{11} M_\odot$.

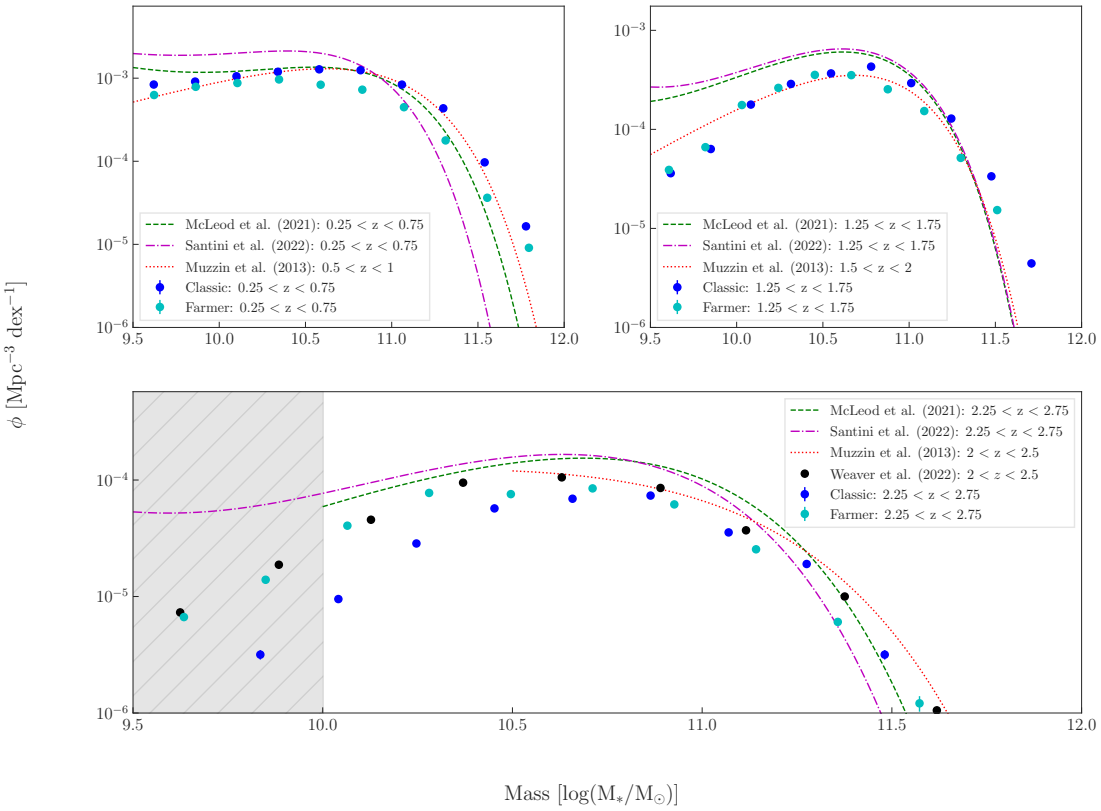

Figure A.3: Similar to Figure A.2, but for the quiescent population. As with our fiducial sample in Figure 3.2, the normalization of our observed SMF is lower than that of McLeod et al. (2021) and Santini et al. (2022), even when using the same redshift bin of $2.25 < z < 2.75$. This difference also persists at lower redshift.

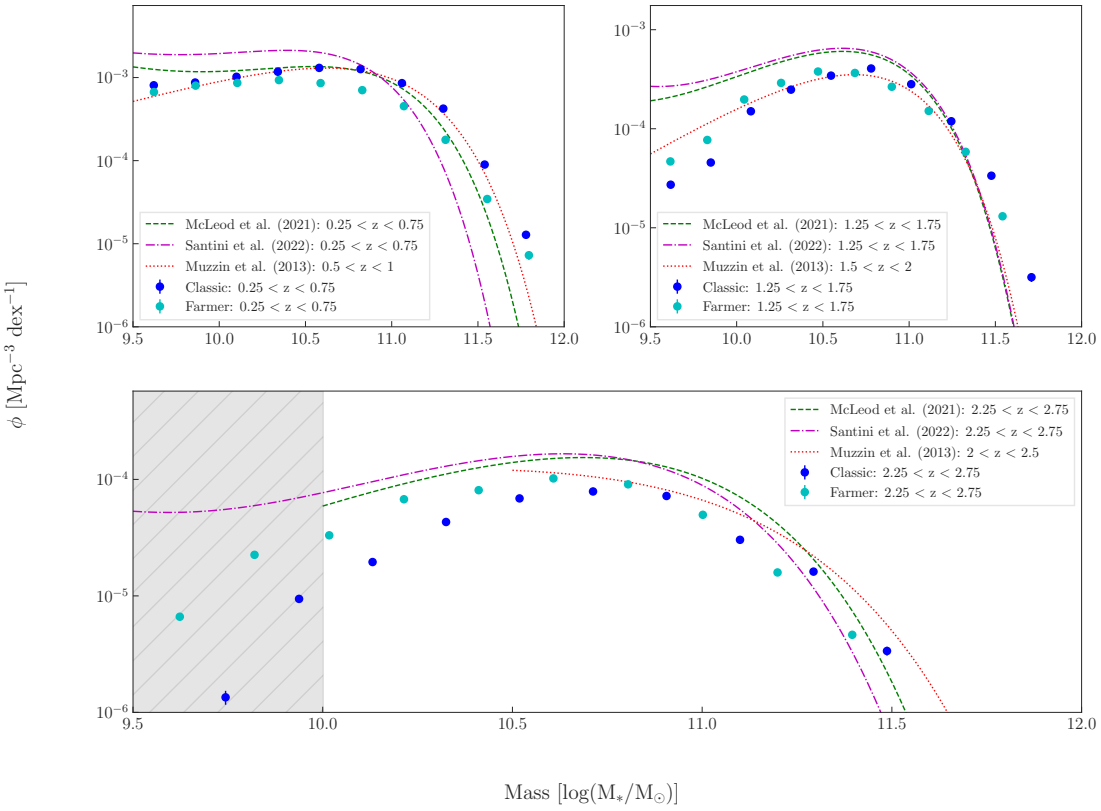

Figure A.4: As Figure A.3, but where quiescent galaxies in our sample are defined from their UVJ colours, rather than the default NUVrJ. This does not remove the discrepancy with McLeod et al. (2021) or Santini et al. (2022), who also use a UVJ colour classification.

Appendix B

Stellar Mass Functions in Different Volumes

In this section we show how the intrinsic protocluster SMFs depend on the different protocluster volume selections tabulated in Table 4.1. These can be compared with our fiducial results, in Figure 4.3. The NUVrJ colour distributions of each sample are shown in Figure B.1. The morphology of the colour distribution is similar for all samples, with the primary difference being one of sample size.

First, in Figure B.2 we show the Core sample, $dR, dz = 0.5$ Mpc, 0.2. As with the fiducial sample, we observe a significant excess of low-mass protocluster galaxies, with an SMF that rises even more steeply towards lower masses. In addition, there is a bump at $M_* \sim 10^{11.25} M_\odot$, corresponding to an excess of very massive galaxies that is not seen in the wider selection. Also different from the fiducial sample is the drop in the number of star-forming (and, hence, total) galaxies at the lowest stellar masses.

Next in Figure B.3 we consider the Core-complete selection ($dR, dz = 0.5, 0.3$). This is similar to the Core sample just discussed, but with a higher completeness due to the larger dz range, chosen to include $\sim 95\%$ of all quiescent galaxies in the cluster (See section 2.3). The results are generally indistinguishable from Figure B.2, though the uncertainties on the quiescent SMF are larger due to the increased field contamination. This demonstrates that the narrower $dz = 0.2$ selection used in our fiducial sample does not significantly bias the results against quiescent galaxies.

Finally, in Figure B.4, we show the Wide selection of $dR = 1.5$ Mpc and $dz = 0.2$. For this volume, the SMFs are in general much more similar in shape to that of the field.

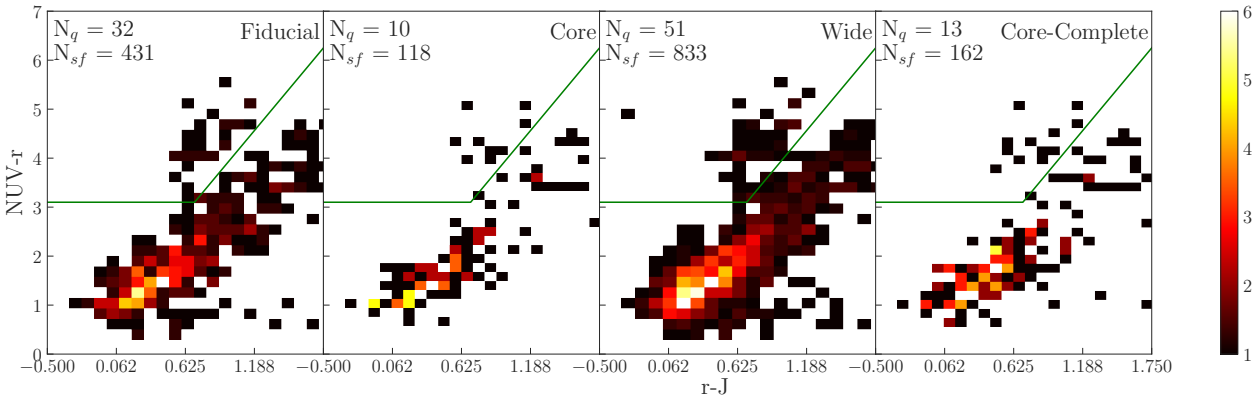

Figure B.1: The (NUV-r) vs. (r-J) colour distribution is shown for each volume selection (Table 4.1). The division between quiescent and star-forming galaxies is shown as the green line. We observe a distinct quiescent population in each selection volume.

.

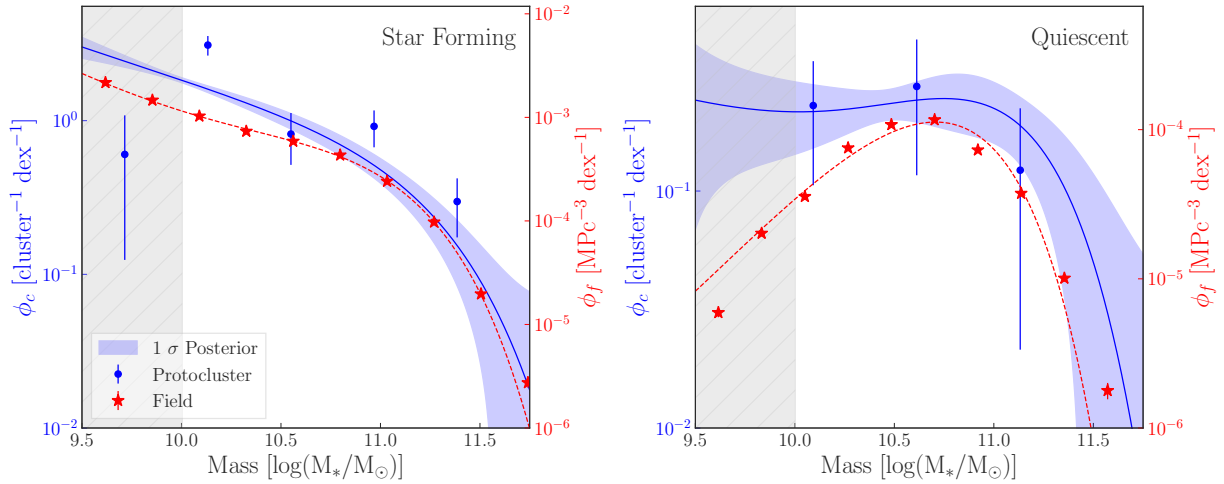

Figure B.2: We show the intrinsic protocluster SMFs for our Core selection ($dR = 0.5$ Mpc, $dz = 0.2$), to be compared with our fiducial results in Figure 4.3. In this sample, the excess of low-mass quiescent galaxies is even more pronounced, with an SMF that increases steeply toward lower masses. There is also an excess of massive, quiescent galaxies, and a deficit of low-mass, star-forming galaxies.

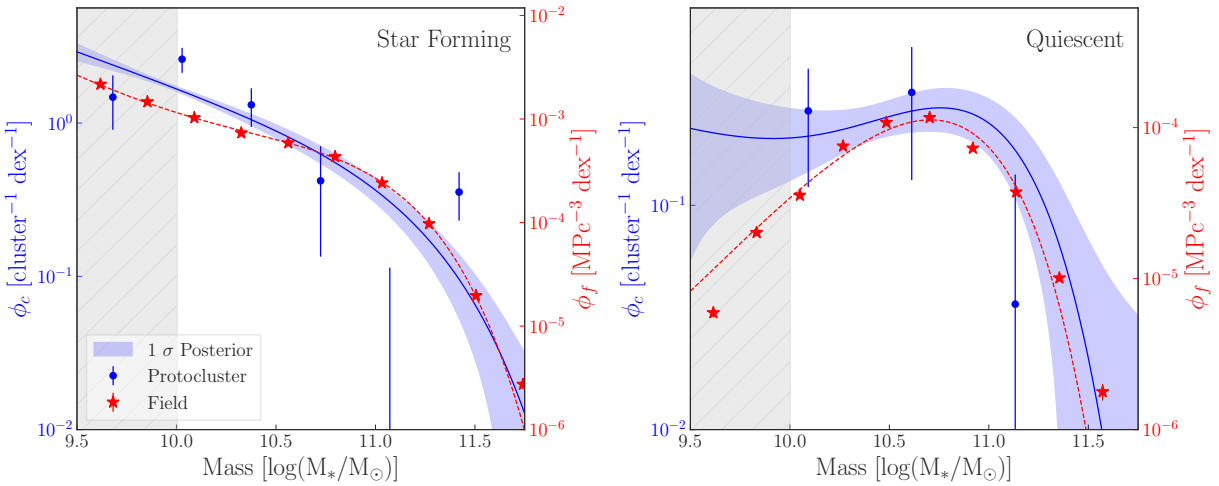

Figure B.3: As Figure 4.3, but for the Core-complete sample ($dR = 0.5$ Mpc, $dz = 0.3$). Results are very similar to the Core sample shown in Figure B.2. Uncertainties on the quiescent SMF are larger because the larger dz results in greater field contribution within the volume.

An excess of low-mass quiescent galaxies is still apparent, though it is not statistically significant.

We also look at the intrinsic protocluster SMF for galaxies with selection parameters $dR = 1$ Mpc, $dz = 0.2$ around just the most massive protocluster in our sample, ZFOURGE/ZFIRE. We note that there are no quiescent galaxies above $10^{10} M_\odot$. However, there is a large low-mass excess in this protocluster; all six quiescent galaxies in this selection have masses below $M_* < 10^{10.6} M_\odot$. Notably, this number of quiescent galaxies is about an order of magnitude larger than the average per cluster when considering the full sample.

We present the fit parameters for the intrinsic protocluster SMFs in each selection, as well as the fit parameters for the field in Table B.1.

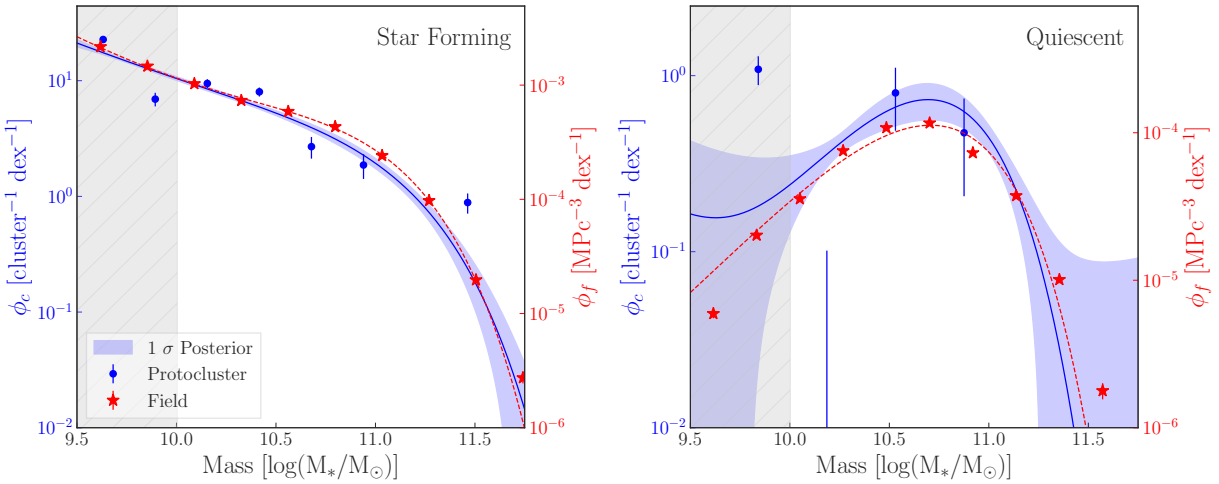

Figure B.4: As Figure 4.3, but for the Wide selection ($dR = 1.5$ Mpc, $dz = 0.2$). The SMF shapes are generally consistent with the field, though the flatter shape of the quiescent SMF in protoclusters is still present.

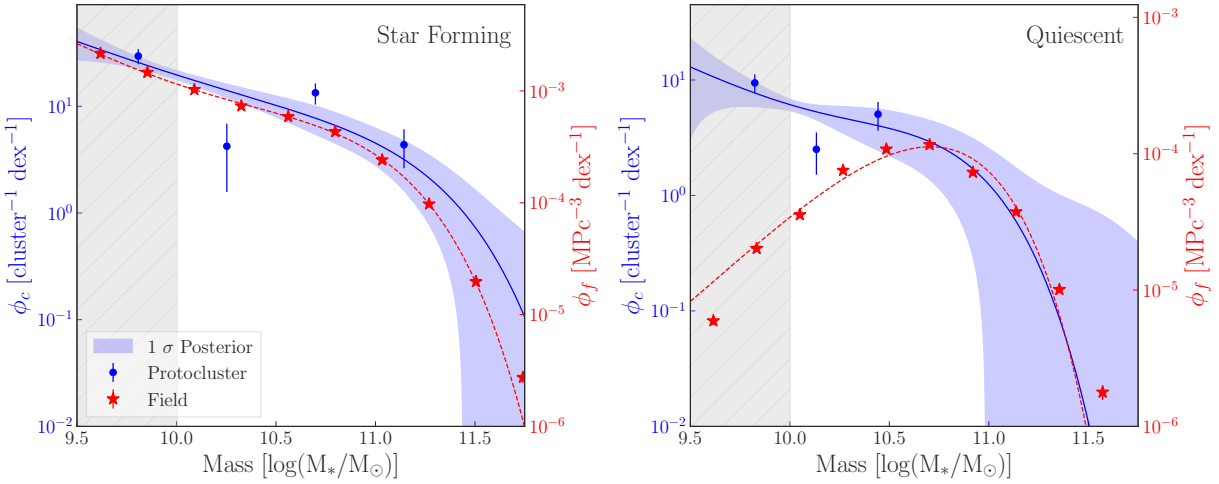

Figure B.5: As Figure 4.3, but for just galaxies with selection parameters $dR = 1$ Mpc, $dz = 0.2$ around just the most massive protocluster in our sample, ZFOURGE/ZFIRE. The number of low-mass quiescent galaxies here is about a factor ten larger than the average for our full sample.

Selection	**Alias**	**Population**	$\mathcal{M}$*	**log**ϕ_1^*	α_1	**log**ϕ_2^*	α_2
A	Fiducial	Total	$10.91^{+0.19}_{-0.16}$	$0.34^{+0.20}_{-0.24}$	$-0.72^{+0.41}_{-0.63}$	$-0.34^{+0.26}_{-0.28}$	$-1.64^{+0.36}_{-0.27}$
		Quiescent	$10.66^{+0.21}_{-0.18}$	$-0.15^{+0.11}_{-0.14}$	$0.16^{+0.61}_{-0.52}$	$-1.11^{+0.32}_{-0.75}$	$-1.21^{+0.15}_{-0.43}$
		Star Forming	$10.95^{+0.19}_{-0.16}$	$0.28^{+0.17}_{-0.28}$	$-0.93^{+0.43}_{-0.38}$	$-0.74^{+0.47}_{-1.07}$	$-1.88^{+0.26}_{-0.75}$
B	Core	Total	$11.20^{+0.31}_{-0.21}$	$-0.45^{+0.27}_{-0.31}$	$-1.12^{+0.54}_{-0.30}$	$-1.10^{+0.34}_{-0.51}$	$-1.53^{+0.26}_{-0.18}$
		Quiescent	$10.95^{+0.41}_{-0.71}$	$-0.66^{+0.17}_{-0.28}$	$-0.12^{+0.95}_{-0.71}$	$-1.54^{+0.30}_{-0.57}$	$-1.27^{+0.18}_{-0.30}$
		Star Forming	$11.22^{+0.37}_{-0.17}$	$-0.58^{+0.19}_{-0.30}$	$-1.24^{+0.51}_{-0.21}$	$-1.29^{+0.34}_{-0.45}$	$-1.59^{+0.38}_{-0.19}$
C	Wide	Total	$10.91^{+0.21}_{-0.11}$	$0.47^{+0.15}_{-0.24}$	$-0.91^{+0.30}_{-0.46}$	$-0.51^{+0.42}_{-0.58}$	$-1.90^{+0.32}_{-0.33}$
		Quiescent	$10.49^{+1.32}_{-0.14}$	$-0.17^{+0.05}_{-0.39}$	$0.60^{+0.59}_{-0.66}$	$-2.05^{+0.82}_{-1.14}$	$-1.81^{+0.65}_{-0.95}$
		Star Forming	$11.00^{+0.17}_{-0.14}$	$0.24^{+0.20}_{-0.23}$	$-1.07^{+0.35}_{-0.40}$	$-0.43^{+0.32}_{-0.56}$	$-1.79^{+0.13}_{-0.28}$
D	Core Complete	Total	$11.19^{+0.24}_{-0.19}$	$-0.54^{+0.23}_{-0.27}$	$-1.27^{+0.41}_{-0.19}$	$-1.18^{+0.33}_{-0.48}$	$-1.50^{+0.28}_{-0.19}$
		Quiescent	$10.77^{+0.43}_{-0.25}$	$-0.60^{+0.12}_{-0.22}$	$0.17^{+0.82}_{-0.72}$	$-1.48^{+0.29}_{-0.79}$	$-1.27^{+0.18}_{-0.37}$
		Star Forming	$11.25^{+0.31}_{-0.23}$	$-0.75^{+0.27}_{-0.34}$	$-1.39^{+0.43}_{-0.19}$	$-1.39^{+0.36}_{-0.51}$	$-1.57^{+0.37}_{-0.20}$
Field		Total	$10.87^{+0.04}_{-0.03}$	$-3.31^{+0.02}_{-0.03}$	$-0.74^{+0.12}_{-0.18}$	$-4.44^{+0.21}_{-0.56}$	$-2.05^{+0.12}_{-0.34}$
		Quiescent	$10.54^{+0.03}_{-0.03}$	$-3.92^{+0.002}_{-0.004}$	$0.46^{+0.09}_{-0.09}$	$-6.88^{+0.53}_{-0.74}$	$-1.30^{+0.23}_{-0.48}$
		Star Forming	$10.90^{+0.05}_{-0.05}$	$-3.45^{+0.03}_{-0.04}$	$-0.80^{+0.26}_{-0.17}$	$-4.37^{+0.31}_{-0.37}$	$-1.98^{+0.16}_{-0.20}$

Table B.1: Summary of best-fit parameters for the double Schechter functions fit to each selection and population. The field is defined as everything between $2 < z < 2.5$, and the fit to the intrinsic protocluster SMF ϕ_c are as described in Section 3.1. $\mathcal{M}^*$ is in units of $\log(M_*/M_\odot)$, and α_1 and α_2 are unitless. ϕ_1^* and ϕ_2^* are in units of $\mathrm{dex}^{-1}\mathrm{cluster}^{-1}$, except for the field, where it is presented in units of $\mathrm{dex}^{-1}\mathrm{Mpc}^{-3}$.